Title

Nuclear morphology is shaped by loop-extrusion programs

Journal

Nature, 627(8002)

ISSN

0028-0836

Authors

Patta, Indumathi

Zand, Maryam

Lee, Lindsay

et al.

Publication Date

2024-03-07

DOI

10.1038/s41586-024-07086-9

Peer reviewed

HHS Public Access

Author manuscript

Nature. Author manuscript; available in PMC 2024 April 26.

Published in final edited form as:

Nature. 2024 March ; 627(8002): 196–203. doi:10.1038/s41586-024-07086-9.

Nuclear morphology is shaped by loop-extrusion programs

Indumathi Patta[1], **Maryam Zand**[2], **Lindsay Lee**[3], **Shreya Mishra**[3], **Alexandra Bortnick**[1], **Hanbin Lu**[1], **Arpita Prusty**[1], **Sara McArdle**[4], **Zbigniew Mikulski**[4], **Huan-You Wang**[5], **Christine S. Cheng**[2], **Kathleen M. Fisch**[6,✉], **Ming Hu**[3,✉], **Cornelis Murre**[1,✉]

[1]Department of Molecular Biology, University of California, San Diego, La Jolla, CA, USA.

[2]Department of Psychiatry, University of California, San Diego, La Jolla, CA, USA.

[3]Department of Quantitative Health Sciences, Lerner Research Institute, Cleveland Clinic Foundation, Cleveland, OH, USA.

[4]Microscopy and Histology Core Facility, La Jolla Institute for Immunology, La Jolla, CA, USA.

[5]Department of Pathology, University of California, San Diego, La Jolla, CA, USA.

[6]Department of Obstetrics, Gynecology and Reproductive Sciences, University of California, San Diego, La Jolla, CA, USA.

Abstract

It is well established that neutrophils adopt malleable polymorphonuclear shapes to migrate through narrow interstitial tissue spaces[1–3]. However, how polymorphonuclear structures are assembled remains unknown[4]. Here we show that in neutrophil progenitors, halting loop extrusion —a motor-powered process that generates DNA loops by pulling in chromatin[5]—leads to the assembly of polymorphonuclear genomes. Specifically, we found that in mononuclear neutrophil progenitors, acute depletion of the loop-extrusion loading factor nipped-B-like protein (NIPBL) induced the assembly of horseshoe, banded, ringed and hypersegmented nuclear structures and led to a reduction in nuclear volume, mirroring what is observed during the differentiation of

✉**Correspondence and requests for materials** should be addressed to Kathleen M. Fisch, Ming Hu or Cornelis Murre. kfish@health.ucsd.edu; hum@ccf.org; cmurre@ucsd.edu.

Author contributions C.M. conceived the study. I.P. and C.M. designed experiments. I.P. performed the vast majority of experiments and analysed data. M.Z., H.L., A.B., A.P., Z.M., C.S.C., K.M.F. and M.H. analysed data, provided technical support and clarified concepts. H.L. analysed ATAC-seq data. M.Z. and C.S.C. analyzed scRNA-seq data. S. McArdle performed nuclear volume measurements. H.-Y.W. identified and quantified neutrophil subsets. L.L., S. Mishra and M.H. performed the Hi-C analysis. The study was supervised by C.S.C., K.M.F., M.H. and C.M. I.P., M.H. and C.M. wrote the manuscript.

Competing interests The authors declare no competing interests.

Reporting summary

Further information on research design is available in the Nature Portfolio Reporting Summary linked to this article.

Online content

Any methods, additional references, Nature Portfolio reporting summaries, source data, extended data, supplementary information, acknowledgements, peer review information; details of author contributions and competing interests; and statements of data and code availability are available at https://doi.org/10.1038/s41586-024-07086-9.

Additional information

Supplementary information The online version contains supplementary material available at https://doi.org/10.1038/s41586-024-07086-9.

Peer review information *Nature* thanks Paul Kubes, Ralph Stadhouders and the other, anonymous, reviewer(s) for their contribution to the peer review of this work.

neutrophils. Depletion of NIPBL also induced cell-cycle arrest, activated a neutrophil-specific gene program and conditioned a loss of interactions across topologically associating domains to generate a chromatin architecture that resembled that of differentiated neutrophils. Removing NIPBL resulted in enrichment for mega-loops and interchromosomal hubs that contain genes associated with neutrophil-specific enhancer repertoires and an inflammatory gene program. On the basis of these observations, we propose that in neutrophil progenitors, loop-extrusion programs produce lineage-specific chromatin architectures that permit the packing of chromosomes into geometrically confined lobular structures. Our data also provide a blueprint for the assembly of polymorphonuclear structures, and point to the possibility of engineering de novo nuclear shapes to facilitate the migration of effector cells in densely populated tumorigenic environments.

Immune surveillance is established and maintained by an armoury of different cell types. The process of identifying these immune cells—lymphocytes, monocytes, eosinophils and neutrophils—began in the late 1880s[6–8]. Metchnikoff defined neutrophils as multilobular cells and proposed that they serve as an inflammatory defence system in humans[6,7] (Fig. 1a). Neutrophils adopt a spectrum of distinct nuclear morphologies in which nuclei appear banded, ring-shaped or hypersegmented. Neutrophil intermediates include myelocytes, metamyelocytes and band neutrophils, which give rise to mature neutrophils and end-stage segmented neutrophils, often referred to as hypersegmented neutrophils or polymorphonuclear neutrophils. The assembly of polymorphonuclear structures requires the expression of the lamin B receptor, an inner-nuclear-membrane protein that tethers heterochromatin to the nuclear lamina[9,10].

Human and mouse mononuclear genomes assemble into chromosome territories that are radially distributed according to gene density[11,12]. In polymorphonuclear cells, chromosomes distribute randomly among nuclear lobes but, on the basis of gene density, adopt a radial chromosomal distribution that mirrors mononuclear cells[13]. At the chromosomal level, evidence suggests that interphase chromosomes are structured as 11-nm nucleosome fibres that coil into flexible 200-nm helical springs[14,15]. Transcriptionally permissive and repressive chromatin are segregated from each other by folding into euchromatic (A) and heterochromatic (B) compartments[16]. At the megabase scale, chromatin folds into bundles of loops that are known as topologically associating domains (TADs) or stacked rosettes[17,18]. TADs and/or rosettes are assembled by the cohesin-mediated extrusion of chromatin[5,19]. The cohesin complex is composed of multiple subunits, including RAD21 (SCC1), STAG and two structural maintenance of chromosomes proteins (SMC1a and SMC3)[5,19]. The cohesin loading factors NIPBL and MAU2 sequester RAD21 across the chromatin landscape[5,20]. SMC1a and SMC3 are DNA translocases that extrude loops until pairs of convergent CTCF sites are reached[19,21]. The release of cohesin from chromatin is orchestrated by WAPL[22].

During development, tissue homeostasis and immune surveillance, cells often need to migrate through complex confined environments. These spatially constrained neighbourhoods are densely populated with cells and associated extracellular matrices, creating labyrinths of interstitial spaces that are often smaller than the size of migrating cells. Neutrophils use amoeboid-like migration to quickly navigate through narrow

accessible trajectories[1,2]. Although emerging data indicate that aberrant changes in nuclear shape and nuclear deformability are linked to a myriad of maladies, including cancer, cardiac disease and immune-cell deficiencies, the molecular programs that instruct nuclear morphology and nuclear malleability remain unknown. As a first approach to identify the molecular determinants that condition nuclear morphology, we used neutrophils as a model system. We found that in neutrophil progenitors, cohesin-dependent looping assembled mononuclear structures, induced cell proliferation and suppressed the induction of a neutrophil-specific gene program. Conversely, halting loop extrusion in neutrophil progenitors instructed the assembly of polymorphonuclear shapes, reduced nuclear volume, induced cell-cycle arrest and activated a neutrophil- and inflammatory-specific transcription signature.

Loop-extrusion factors decline in neutrophils

In previous studies, we used an in vitro culture system involving a myeloid progenitor cell line, named ECOMG, to determine how polymorphonuclear structures are assembled[23,24] (Fig. 1b). ECOMG cells are mononuclear cells that can be expanded indefinitely when cultured in the presence of β-oestradiol but which, when β-oestradiol is withdrawn, undergo cell-cycle arrest, differentiate into polymorphonuclear neutrophils and are associated with large-scale changes in chromatin architecture including a decline in intra-TAD interactions[24] (Fig. 1b, Extended Data Fig. 1a–c and Supplementary Table 1). These observations raised the possibility that neutrophil differentiation is associated with a decline in loop-extrusion activity. To investigate this possibility, we monitored the expression of SMC1a, SMC3, RAD21, NIPBL, MAU2 and WAPL in ECOMG progenitors and ECOMG-derived neutrophils. We found that the transcript abundance of *Smc1a*, *Smc3*, *Rad21* and *Nipbl*, but not that of *Mau2* or *Wapl*, declined after the withdrawal of β-oestradiol (differentiated neutrophils) (Fig. 1c). To determine whether the decrease in transcript abundance correlated with a decrease in protein levels, we performed western blotting. We found that in ECOMG-derived differentiated neutrophils, the protein levels of SMC1, SMC3, RAD21 and NIPBL remained detectable, but overall mirrored the decline in mRNA abundance (Extended Data Fig. 1d). The transcript levels of *Smc1a*, *Smc3* and *Rad21*, but not those of *Nipbl*, *Mau2* and *Wapl*, declined in differentiating bone marrow neutrophils[25] (Extended Data Fig. 1e). We conclude that the expression of a subset of genes encoding factors that promote loop extrusion declines in differentiating neutrophils.

Loss of NIPBL induces a neutrophil cell fate

To investigate whether declining levels of loop-extrusion factors instruct neutrophil differentiation, we used ECOMG progenitors that carry an inducible NIPBL-FKBP12^{F36V}-EYFP degron inserted into the endogenous *Nipbl* locus[26] (Fig. 1b). We found that NIPBL-FKBP12^{F36V}-EYFP progenitors, when cultured with a cell-permeable compound (dTAG-13) that initiates the degradation of FKBP12^{F36V}-conjugated proteins, were depleted for NIPBL[26,27] (Fig. 1d,e). To determine whether the removal of NIPBL modulates cell proliferation and neutrophil differentiation, we examined NIPBL-FKBP12^{F36V}-EYFP progenitors cultured with β-oestradiol and in the absence or presence of dTAG-13 for cell-cycle progression and for the expression of cell-surface markers that define a neutrophil

cell fate. We found that depletion of NIPBL caused cell-cycle arrest, increased cell death and induced the expression of surface markers that define neutrophil identity (Fig. 1d and Extended Data Fig. 2a,b). Notably, depletion of NIPBL swiftly activated the expression of genes encoding transcription factors that establish neutrophil identity, and modulated the expression of genes that are involved in establishing the architecture of the nuclear envelope (Fig. 1f–h, Extended Data Fig. 2c and Supplementary Table 2). To determine whether depletion of MAU2 also induces neutrophil differentiation, we examined ECOMG progenitors that carried MAU2-FKBP12^{F36V}-mScarlet degrons[26]. Depletion of MAU2 also activated a neutrophil-specific transcription signature, albeit significantly less so when compared to NIPBL-depleted cells (Extended Data Fig. 2d–f and Supplementary Table 3). Combined depletion of NIPBL and MAU2 activated a neutrophil-specific transcription signature that mirrored NIPBL depletion alone (Extended Data Fig. 2g–i and Supplementary Table 4). To determine whether depletion of NIPBL orchestrates the assembly of polymorphonuclear shapes, NIPBL-FKBP12^{F36V}-EYFP progenitors grown with β-oestradiol and in the absence or presence of dTAG-13 were examined for nuclear morphology using Wright–Giemsa staining. NIPBL-FKBP12^{F36V}-EYFP progenitors were mononuclear, but when depleted for NIPBL, they swiftly adopted polymorphonuclear structures that included myelocytes, metamyelocytes, band neutrophils and mature neutrophils (Fig. 2a,b). Particularly striking were NIPBL-depleted cells that adopted multiple but continuous spatially distinguished nuclear lobes, a signature normally associated with terminally differentiated hypersegmented neutrophils (Fig. 2a,b). To further validate whether NIPBL depletion modulates RAD21 occupancy, we examined RAD21 occupancy in NIPBL-depleted cells. We found that NIPBL-depleted progenitors were depleted for RAD21 at sites associated with CTCF occupancy (Extended Data Fig. 3). To determine whether RAD21 depletion also instructs the assembly of polymorphonuclear structures we examined ECOMG cells that carried a RAD21-FKBP12^{F36V}-EYFP degron[26]. RAD21-depleted cells cultured with dTAG-13 for 36 h showed extensive cell death but differentiated into polymorphonuclear cells that expressed increased levels of CD11b and, albeit to a lesser extent, Ly6G (Extended Data Fig. 4). We conclude that halting loop extrusion in neutrophil progenitors activates a neutrophil-specific gene program and instructs the assembly of polymorphonuclear shapes.

Neutrophil chromatin mirrors the loss of NIPBL

To determine whether halting loop extrusion modulates chromatin accessibility, we performed assay for transposase-accessible chromatin with sequencing (ATAC-seq) in NIPBL-FKBP12^{F36V}-EYFP progenitors cultured with β-oestradiol and in the absence or presence of dTAG-13. For differential peak analysis, we compared peaks detected at 72 h only, 0 h only and overlapping subsets. NIPBL-depleted cells showed increased chromatin accessibility at promoters and enhancers enriched for binding sites for Ikaros, PU.1, AP-1, BATF, ETS and CEBP (Extended Data Fig. 5a,b,e). Conversely, NIPBL depletion severely reduced chromatin accessibility at sites that span the *Myc* locus, consistent with the steep decline in *Myc* transcript abundance and cell-cycle arrest (Extended Data Fig. 5c–e). To examine whether halting loop extrusion instructs the assembly of a distinct chromatin architecture, we performed a genome-wide chromosome-conformation capture assay (Hi-C).

We found that NIPBL-FKBP12^{F36V}-EYFP cells cultured with β-oestradiol and dTAG-13 were depleted for local intrachromosomal contact frequencies (<4 Mb) but enriched for remote intrachromosomal frequencies (>4 Mb) (Fig. 3a). Consistent with previous results, NIPBL depletion increased compartmentalization and segregation strength[20] (Extended Data Fig. 6a,b and Supplementary Tables 5 and 6). As expected, ECOMG cells that were cultured in the presence of β-oestradiol and dTAG-13 showed a significant decline in intra-TAD interactions (Fig. 3b, left). ECOMG cells that after β-oestradiol withdrawal differentiated into neutrophils also showed a significant decrease in intra-TAD interactions (Fig. 3b, right). The reduction in intra-TAD interactions of differentiated neutrophils mirrored that of NIPBL-depleted ECOMG progenitors (Fig. 3b,c). Chromosome-wide KR-normalized contact matrices for NIPBL-depleted cells also resembled those for ECOMG-derived differentiated neutrophils (Fig. 3d). We found that both NIPBL-depleted cells and differentiated neutrophils showed a decline in intra-TAD domain interactions but an increase in long-range genomic interactions when compared with progenitor cells (Fig. 3b–f). Meta-TAD and meta-loop plots confirmed that intra-TAD contact frequencies and loop strength declined in NIPBL-depleted cells and, to a lesser degree, in ECOMG-derived differentiated neutrophils (Fig. 3g,h). To determine how halting loop extrusion instructs alterations in gene expression, we examined ECOMG progenitors and NIPBL-depleted ECOMG progenitors for changes in chromatin folding. We found that NIPBL depletion orchestrated a massive loss of 9,010 loops versus a gain of 4,145 loops (Extended Data Fig. 6c and Supplementary Table 7). In NIPBL-depleted cells, genes that were associated with decreased mRNA abundance were predominantly depleted for loops (Extended Data Fig. 6d,g). Genes that after depletion of NIPBL showed an increase in transcript abundance showed both loss and gain of loops (Extended Data Fig. 6d,h). To determine how the gain of loops relates to the assembly of promoter–enhancer interactions, we searched for promoter regions that were associated with gained loops. We identified an ensemble of genes (171) that were associated with gained loops (190) and showed enrichment for corresponding promoter–enhancer interactions (944) (Supplementary Table 8). We found that this subset of genes was closely associated with an inflammatory gene program and a neutrophil-specific enhancer repertoire (Extended Data Fig. 6e,f). Collectively, these data indicate that, in neutrophil progenitors, NIPBL depletion instructs a neutrophil-specific chromatin architecture and assembles de novo loops to activate a neutrophil-specific gene program.

Loss of NIPBL induces mega-loops

The data above indicate that depletion of NIPBL is associated with large-scale changes in looping that involve both local and remote genomic interactions. Further inspection of the distribution of loop sizes revealed that, upon depletion of NIPBL, a large fraction of the lost and gained loops spanned vast genomic distances (>5 Mb) (Supplementary Table 9). We will refer to this subset of loops as mega-loops. NIPBL-depleted cells gained 891 mega-loops but lost 102 mega-loops (Supplementary Table 9). Mega-loops tethered at the heterochromatic (B) compartments spanned on average larger intervening DNA sequences than did mega-loops located in the euchromatic (A) compartments (Fig. 4a). In NIPBL-depleted cells, we observed a significant decline in intra-TAD contact frequencies across genomic regions that spanned gained mega-loops (Fig. 4b and Supplementary Table 10).

When NIPBL was removed, gained mega-loops were associated with both increased and decreased mRNA levels, whereas lost mega-loops were mainly associated with declining mRNA abundance (Fig. 4c). Genes that spanned euchromatic mega-loop anchors were enriched for an inflammatory-specific gene program (Fig. 4d,e and Supplementary Tables 11 and 12). Putative regulatory elements at mega-loop anchors that showed altered chromatin accessibility in NIPBL-depleted cells were enriched for PU.1 (SPI1), Ikaros and CTCF binding sites[28–30] (Fig. 4f,g). To determine whether and how the assembly of mega-loops mechanistically relates to gene expression, we zoomed in on mega-loop anchors associated with inflammatory and neutrophil transcription. Specifically, we focused on the *Nlrp3* and *Sec14l1* loci (Fig. 4h and Extended Data Fig. 7). NLRP3 is the key component of the inflammasome, a sensor that activates an inflammatory response if foreign antigens are detected[31,32]. SEC14L1 has a role in innate antiviral signalling[33]. We found that *Nlrp3* was amongst the most differentially expressed genes induced in NIPBL-depleted cells as well as in differentiated neutrophils (Supplementary Tables 1 and 2). In NIPBL-depleted cells, intra-TAD interactions were reduced across loop bodies that paired the *Nlrp3* and *Sec14l1* loci (Extended Data Fig. 7a,b). The depletion of TADs across mega-loop bodies was accompanied by an enrichment for remote genomic interactions at mega-loop anchors (Fig. 4h). NIPBL-depleted cells showed an increase in mRNA abundance and chromatin accessibility, although not uniformly, across the *Nlrp3* and *Sec14l1* loci (Extended Data Fig. 7c,d). Together, these data indicate that in neutrophil progenitors, halting loop extrusion pairs distally located enhancers and promoters in shared transcription hubs.

Gain of interchromosomal contact hubs

To determine whether depletion of NIPBL modulates interchromosomal interactions, we computed interchromosomal contact frequencies for NIPBL-FKBP12^{F36V}-EYFP progenitors cultured in the absence or in the presence of dTAG-13. We found that NIPBL depletion significantly enriched for interchromosomal contacts (Extended Data Fig. 8a and Supplementary Table 13). We next focused our analysis on the top 447 genomic regions that were enriched in NIPBL-depleted cells (Supplementary Table 14). Although all autosomes gained interaction frequencies, chromosomes 5, 7, 8, 11 and 17 showed particular enrichment (Extended Data Fig. 8b,c and Supplementary Table 14). Interchromosomal interactions were particularly prevalent in gene-rich chromosomes that spanned the euchromatic (A) compartment (Extended Data Fig. 8c,d and Extended Data Fig. 9). We identified 3,951 genes that were associated with interchromosomal hubs, of which 1,475 genes were differentially expressed in NIPBL-depleted cells (Extended Data Fig. 8e and Supplementary Tables 15 and 16). Gene ontology (GO) enrichment analysis revealed a significant enrichment for genes associated with neutrophil physiology and inflammation (Extended Data Fig. 8f and Supplementary Table 17). Transcript abundance and chromatin accessibility for genes associated with a neutrophil-specific gene program, including *Trem1*, *Ptprj* and *Spi1*, were significantly increased in NIPBL-depleted cells (Extended Data Fig. 8g). Finally, we found that gained chromatin-accessible regions at interchromosomal hubs were enriched for binding sites for Ikaros, PU.1 and AP-1, whereas reduced chromatin-accessible regions were enriched for binding sites for CTCF and BORIS (Extended Data Fig. 8h,i). The assembly of mega-loops and gain of interchromosomal

hubs in NIPBL-depleted cells raised the possibility that such interactions are established to facilitate the packing of chromosomes into confined geometric polymorphonuclear structures. To determine whether halting loop extrusion instructs the assembly of constrained nuclear space, we measured the nuclear volumes of NIPBL-FKBP12^{F36V}-EYFP progenitors cultured in the absence or presence of dTAG-13. We found that depletion of NIPBL led to significant reductions in the nuclear volumes of progenitors, similar to what is observed in differentiated neutrophils[24] (Extended Data Fig. 8j). We conclude that nuclear volumes are regulated by loop-extrusion programs.

Loss of NIPBL in primary progenitors

To determine whether halting loop extrusion also converts primary bone-marrow-derived mononuclear progenitors into differentiated polymorphonuclear cells, we generated CRISPR RNAs (crRNAs) that target NIPBL–MAU2 heterodimerization[34,35] (Supplementary Table 18). crRNAs and Cas9 protein were mixed with ATTO-550-conjugated transactivating crRNAs (tracrRNAs) and electroporated into ECOMG progenitors[36,37]. Consistent with the results in NIPBL-FKBP12^{F36V}-EYFP cells that were incubated with dTAG-13, a noticeable fraction of progenitor cells electroporated with either Cas9–NIPBL-crRNA1–tracrRNA (crRNP-1) or Cas9–NIPBL-cRNA2–tracrRNA (crRNP-2) expressed CD11b and Ly6G (Extended Data Fig. 10a–c). Next, to ablate the expression of NIPBL in neutrophil progenitors derived from the bone marrow, we combined crRNP-1 and crRNP-2 to target NIPBL expression. Specifically, lineage-negative haematopoietic progenitors were enriched from the bone marrow, electroporated with NIPBL-targeting crRNP-1 and crRNP-2 and cultured for 72 h in the presence of SCF and FLT3L. We found that the ATTO-550-positive (ATTO-550^{+}) fraction was significantly enriched for cells that expressed CD11b (76%) or both CD11b and Ly6G (16.3%) (Extended Data Fig. 10d,e). Notably, primary neutrophil progenitors electroporated with NIPBL-targeting crRNP-1 and crRNP-2 (ATTO-550^{+}) were depleted for precursors (6.8%), myelocytes (12.2%) and metamyelocytes (9.4%), but enriched for band neutrophils (47%) and mature neutrophils (19%), as well as hypersegmented neutrophils (5%) (Extended Data Fig. 10f). Together, these data indicate that depletion of NIPBL in primary bone-marrow-derived haematopoietic progenitors fosters the expression of neutrophil-associated cell-surface markers and the assembly of polymorphonuclear structures. To determine whether NIPBL depletion in bone-marrow-derived haematopoietic progenitors activates a neutrophil-specific gene program, we analysed more than 15,000 single cells per replicate using single-cell RNA sequencing (scRNA-seq). To identify distinct clusters of cells, a composite two-dimensional uniform manifold approximation and projection (UMAP) plot of expression profiles for two replicates of ATTO-550^{-} and ATTO-550^{+} populations was generated (Extended Data Fig. 11a). Most of the selected genes mapped to distinct myeloid and neutrophil progenitors, as well as to mature neutrophils[38] (Extended Data Fig. 11b–d). To determine whether depletion of NIPBL enriched the development of neutrophils, we compared the UMAP plots derived from integration and clustering of two replicates of ATTO-500^{-} (control) and ATTO-550^{+} (NIPBL-depleted) populations as well as bone-marrow-derived neutrophils (Extended Data Fig. 11e). We found that the granulocyte–monocyte progenitor (GMP) compartment was depleted in the ATTO-550^{+} population (Extended Data Fig. 11e,f).

Conversely, NIPBL-depleted cells were enriched for a differentiating neutrophil population, revealing transcripts that clustered with bone-marrow-derived neutrophils[25] (Extended Data Fig. 11e,f). Cellular dynamics analyses showed the trajectories emanating from two distinct origins (Extended Data Fig. 11g). NIPBL depletion substantially increased the abundance of transcripts associated with a neutrophil-specific gene program in neutrophil progenitor cells including GMPs, transitional neutrophils and myeloblasts (Extended Data Fig. 12a–f). Finally, a dominant trajectory originated in GMPs and in myeloblasts or promyelocytes to promote differentiation into myelocytes and immature and mature neutrophils (Extended Data Fig. 11g,h). These data indicate that halting loop extrusion in primary bone-marrow-derived haematopoietic progenitors activates a neutrophil-specific gene program.

Discussion

Metchnikoff described microphages (that is, neutrophils) as ‘distinguished by having a nucleus, which, although single, is divided into several lobes’ over 140 years ago[6]. Since this cardinal discovery, insights into mechanisms that underpin the assembly of polymorphonuclear structures have been lacking. Here we show that in ECOMG neutrophil progenitors, halting loop extrusion is sufficient to activate a neutrophil-specific gene program and to induce the assembly of polymorphonuclear structures. These findings raise the question of how loop-extrusion activity is regulated during the course of neutrophil differentiation. We found that the expression of a subset of loop-extrusion factors, including RAD21, SMC1a and SMC3, declined in differentiating neutrophils, whereas that of other factors, including MAU2 and WAPL, remained unchanged. A careful analysis of the activity of loop-extrusion factors in primary neutrophil progenitors and differentiated progeny will be required to determine how a neutrophil-specific chromatin architecture, depleted for TADs and intra-TAD interactions, is established.

Another outstanding question is how halting loop extrusion activates a neutrophil-specific gene program. In NIPBL-depleted progenitors, the massive loss of loops correlated with transcriptional silencing, whereas the gain of loops was associated with both the repression and the activation of gene expression. In NIPBL-depleted cells, the loss of loops might spatially segregate promoters away from enhancers to silence the expression of downstream target genes. For example, in NIPBL-depleted cells, loss of loops across the *Myc* locus seems to reposition distally located enhancers away from the *Myc* promoter. Conversely, in NIPBL-depleted cells, de novo loops might bring enhancers and promoters that, in progenitors, are segregated from each other at different loops, into close spatial proximity. This effect would activate the expression of a selective group of genes encoding an ensemble of transcription factors that specify neutrophil cell fate, including SPI1, Ikaros, NFIL3 and CEBP, and these transcription factors would, in turn, induce the expression of thousands of genes that establish neutrophil cell fate.

Perhaps the most notable feature of our findings was that halting loop extrusion was sufficient to bring about the assembly of polymorphonuclear structures. Depletion of loop extrusion in other cell types, including embryonic stem cells, liver cells, macrophages and cortical and hippocampal neurons, did not yield polymorphonuclear structures[39–41]. This raises the question of why the loss of loop extrusion in neutrophil mononuclear

progenitors, but not in other cell types, instructs the building of polymorphonuclear shapes. We found that halting loop extrusion in neutrophil progenitors activated the expression of factors that restructure the nuclear envelope. It is possible that changes in the activities of these proteins alter the structure and dynamics of the nuclear envelope to permit the assembly of polymorphonuclear structures[42]. However, this explanation seems too simple to be correct. Instead, we suggest that the assembly of polymorphonuclear structures is orchestrated by lineage-specific transcription factors. Lineage-specific transcription factors may act at enhancers that are positioned at tethers of paired mega-loop anchors[43] and at interchromosomal contact hubs[44]. We found that binding sites for both PU.1 and Ikaros were particularly enriched at enhancers positioned at mega-loop anchors, as well as at interchromosomal hubs. Recent studies have suggested that Ikaros has a key role in establishing lineage-specific mega-loops across B cell genomes[45]. Hence, we propose that Ikaros and SPI1 instruct the deposition of epigenetic marks across enhancers at mega-loops and at interchromosomal hubs to permit the packing of chromosomes in spatially confined multilobular structures (Extended Data Fig. 12g). Other innate immune cells, including eosinophils, basophils and mast cells, also adopt a suite of polymorphonuclear structures. How these differences in nuclear structures are established has yet to be determined. We suggest that the wide variety in nuclear morphologies adopted by innate immune cells and other cells is instructed by lineage-specific loop-extrusion programs. Lineage-specific loop-extrusion programs, in turn, assemble an spectrum of lineage-specific mega-loops and interchromosomal hubs to orchestrate the formation of lineage-specific nuclear shapes (Extended Data Fig. 12g). In sum, our data provide a blueprint for the assembly of polymorphonuclear structures and highlight the possibility of engineering de novo nuclear shapes. We hypothesize that the assembly of new nuclear morphologies permits immune effector cells or other mononuclear cell types to migrate with relatively greater ease into densely populated tumorigenic environments.

Methods

Cell culture

ECOMG progenitors were maintained at 37 °C in a humidified incubator with 5% CO_2. ECOMG progenitors were cultured in RPMI 1640 supplemented with 10% fetal bovine serum (FBS), 1× penicillin–streptomycin–glutamine and 10 ng ml^{-1} GM-CSF; β-oestradiol (E2758, Sigma) was added to the medium at a final concentration of 1 μM from a 10,000× stock in 100% ethanol[23,24]. Acute depletion of NIPBL, MAU2 or RAD21 was achieved by culturing ECOMG progenitors with β-oestradiol and 0.5 μM dTAG-13 (Tocris)[26,27].

Transfection of ECOMG progenitors with Cas9–crRNA–tracrRNA particles

ECOMG progenitors were electroporated with Cas9–crRNA–tracrRNA complexes using a Neon transfection system (Invitrogen). Approximately 1×10^6 cells were washed twice with sterile 1× phosphate-buffered saline (PBS) and resuspended in R buffer (Neon Transfection System 100 μl kit, Thermo Fisher Scientific). Cas9–crRNA–tracrRNA complexes were added to the cells and incubated for 3–5 min at room temperature. Cells were electroporated using the following conditions: voltage, 1,600; width, 10 ms; pulses, 3. Immediately after

electroporation, cells were cultured for 72 h in complete Opti-MEM medium supplemented with 10% FBS.

Electroporation of Cas9–crRNA–tracrRNA particles into bone-marrow-derived lineage-negative progenitors

Six-to-ten-week-old male C57BL/6 mice were euthanized to obtain tibias and femurs, and were used for the isolation of bone marrow cells. Lineage-negative cells were enriched by two-step negative selection. Neutrophils were depleted by labelling bone marrow cells with biotin-tagged Ly6G (1A8, BioLegend) followed by incubation with anti-biotin microbeads (Miltenyi Biotec). The Ly6G-depleted population was enriched for lineage-negative cells by incubating cells with biotin-tagged antibodies obtained from BioLegend: Ly6G (1A8), CD3 (17A2), B220 (RA3–6B2), Ter-119, CD115 (AFS98), F4/80 (BM8), Siglec-F (S17007L) and CD11c (N418), followed by negative selection using anti-biotin microbeads. Enriched lineage-negative cells were collected and electroporated with Cas9–crRNA–tracrRNA complexes immediately after isolation. We used chemically modified synthetic gene-specific crRNAs in conjunction with tracrRNA and Cas9 to target distinct genomic regions of NIPBL (Supplementary Table 18). tracrRNAs fluorescently conjugated to ATTO-550 were used to track transfection efficiencies. We designed four crRNAs (crRNA1, crRNA2, crRNA3 and crRNA4) that target NIPBL. NIPBL-crRNAs as well as control crRNA were obtained from Integrated DNA Technologies (IDT). To prepare crRNA–tracrRNA duplexes, RNA oligos were reconstituted to 100 μM in 100 μl nuclease-free duplex buffer (IDT). RNA oligos were annealed by incubation at 95 °C for 5 min followed by slowly cooling to room temperature for 1 hour[36,37]. The crRNA–tracrRNA duplexes were mixed with Cas9 (QB3 Berkeley Lab) at a 3:1 molar ratio and incubated at room temperature for 20 min. Approximately, 2×10^6 lineage-negative bone marrow precursor cells were resuspended in P3 buffer (P3 Primary Cell 4D-Nucleofector, Lonza), and Cas9–crRNA tracrRNA complexes were electroporated into cells using a Lonza 4D-Nucleofector system (DN-107 program)[36,37]. After electroporation, cells were cultured with 25 ng ml^{-1} SCF and 25 ng ml^{-1} Flt3L (PeproTech) in complete Opti-MEM medium supplemented with 10% FCS for 72 h.

Wright–Giemsa staining

ECOMG cells (0.3×10^6–0.5×10^6) were spun onto slides (Apex Superior Adhesive Slides, Leica) using a Cytospin3 (Shandon, 74010121 GB) for 5 min at 800 rpm, followed by drying at room temperature. Slides were stained using the Kwik-Diff Stain Kit (Thermo Fisher Scientific). In brief, cells were dipped five times in solution 1, three times in solution II and three times in solution III. Slides were washed with H_2O until excess stain was removed, followed by washing in 1× PBS (pH = 6.5). Slides were dried and then mounted using Cytoseal 60 mounting medium (Thermo Fisher Scientific). A Keyence BZX microscope was used for imaging (40× ocular lens and 100× oil immersion objective lens).

Nuclear volumes

Nuclear volumes were quantified using confocal microscopy. Cells were gently scraped off plastic culture plates, fixed with 4% paraformaldehyde and then stained with Hoechst (50 μg ml^{-1}). Stained cells were allowed to settle onto #1.5 cover glasses for 20 min and then mounted onto slides using Prolong Gold. Images were acquired using a Zeiss LSM 980

confocal microscope with the Airyscan2 array detector in super-resolution mode using a 63× (1.4 NA) oil objective. 3D Airyscan processing was performed with a filter strength of 9.0. Images were analysed in Imaris (Bitplane, v.9.7). Nuclei were segmented using the Surface tool using two-pixel smoothing, with identical settings in all cases. Statistical comparisons were performed in Prism (GraphPad, v.9) using an unpaired *t*-test.

Flow cytometry

Single-cell suspensions of ECOMG cells and mouse primary bone marrow cells were prepared. Cells were counted and the cell number was adjusted to 1×10^6–5×10^6 cells per ml using ice-cold FACS buffer (1× PBS with 2% FCS, 1 μM EDTA and 0.1% sodium azide). Approximately 100 μl cell suspension was used for staining with optimal dilutions for the indicated antibodies. The following fluorescently labelled antibodies were used for surface staining: APC anti-Ly-6G/Ly-6C (RB6–8C5), APC anti-Ly-6G (1A8), APC-Cy7 anti-CD11b (M1/70), Brilliant Violet 421 anti-CD11b (M1/70), FITC anti-CD11c (N418), FITC anti-CD3 (17A2), FITC anti-CD4 (GK1.5), FITC anti-CD8a (53–6.7), FITC anti-NK-1.1 (PK136), FITC anti-CD19 (MB19–1), FITC anti-TER-119, FITC anti-CD45R (B220) (RA3–6B2) and Fixable Viability Dye eFluor 780. After staining, cells were washed with 3 ml ice-cold FACS buffer and resuspended in 1 ml of FACS buffer for flow cytometry or in 1–3 ml of FACS buffer for sorting. Intracellular staining of Ki-67 (APC anti-Ki-67, SolA15) was performed using the Foxp3/Transcription Factor Staining Buffer Kit (Tonbo Biosciences). The profiling of cell cycle was performed by fixing cells in 70% ethanol and further incubating with 5 μl propidium iodide (1 mg ml^{-1}). Flow cytometry was performed using a BD LSRFortessa X-20, and fluorescence-activated cell sorting (FACS) analyses were performed using FlowJo v.10.8.1. Sorting of cells was performed using a FACSAria.

Western blotting

NIPBL-FKBP12^{F36V}-EYFP progenitors were cultured in the presence or in the absence of β-oestradiol for 72 h. Cells were collected and lysed in RIPA lysis buffer supplemented with protease inhibitor cocktails and PMSF. Proteins were fractionated using 4–20% pre-cast protein gels. Western blotting was performed using PVDF membranes, followed by incubating overnight at 4 °C with the following antibodies: anti-NIPBL (C-9) (sc-374625, Santa Cruz), anti-RAD21 (ab992, Abcam), anti-SMC3 (ab9263, Abcam) or anti-SMC1 (A300–055A, Bethyl Laboratories). Membranes were stripped and incubated with anti-β-actin (13E5) (Cell Signaling Technology) overnight at 4 °C. Immunoblots were developed by applying SuperSignal West Pico PLUS Chemiluminescent Substrate (Thermo Fisher Scientific), and SuperSignal West Femto Maximum Sensitivity Substrate (Thermo Fisher Scientific). Visualization was done using a BioRad ChemiDoc Imaging System.

RNA-seq

Cells were washed twice with ice-cold 1× PBS and lysed in RLT buffer, a component of RNeasy Plus Mini Kit (Qiagen), with the addition of 10 μl 2-mercaptoethanol per 1 ml of RLT lysis buffer. Total RNA was purified according to the manufacturer's instructions. RNA-seq libraries were generated using the Illumina Ribo-Zero Plus rRNA Depletion Kit, and with IDT for Illumina RNA UD Indexes. Samples were processed following the manufacturer's instructions. The resulting libraries were multiplexed and sequenced

with 100-bp paired-end reads (PE100) to a depth of approximately 25 million reads per sample on an Illumina NovaSeq 6000. Samples were demultiplexed using bcl2fastq v.2.20 Conversion Software (Illumina).

ATAC-seq

ECOMG progenitors expressing NIPBL-FKBP12^{F36V}-EYFP were cultured in the presence or absence of dTAG-13 and were frozen and stored at −80 °C in complete RPMI medium supplemented with 10% FBS and 10% dimethyl sulfoxide. Approximately 50,000 cells were used for ATAC-seq, which was performed according to the manufacturer's instructions for the ATAC-Seq Kit (Active Motif). In brief, cells were centrifuged at 500*g* for 5 min at 4 °C and thoroughly resuspended in ATAC lysis buffer. Nuclei were pelleted immediately by centrifugation at 500*g* at 4 °C for 10 min. Isolated nuclei were subjected to tagmentation in 50 µl ice-cold tagmentation mix containing 2× tagmentation buffer, 10× PBS, 0.5% digitonin, 10% Tween 20 and assembled transposomes. The tagmented DNA was purified using the MinElute PCR Purification Kit (Qiagen). Libraries were constructed by amplifying the tagmented DNA using the Illumina Nextera adapters with primer extension at 72 °C for 5 min and denaturation at 98 °C for 30 s, followed by 10 cycles of denaturation at 98 °C for 10 s, annealing at 63 °C for 30 s and extension at 72 °C for 60 s. The amplified libraries were purified and subjected to SPRI bead selection. The final libraries were quantified and sequenced with 100-bp paired-end reads (PE100) to a depth of approximately 150 million reads per sample on an Illumina NovaSeq 6000.

ChIP–seq

ECOMG progenitors expressing NIPBL-FKBP12^{F36V}-EYFP were cultured in the presence or absence of dTAG-13 for 72hrs. Cells were fixed with 1% formaldehyde for 10 min at room temperature. The reaction was quenched with glycine to a final concentration of 125 mM for 5 min at room temperature. Chromatin immunoprecipitation followed by sequencing (ChIP–seq) was performed using the ChIP-IT High Sensitivity Kit (Active Motif) according to the manufacturer's instructions. In brief, cells were resuspended in chromatin preparation buffer and incubated on ice for 10 min. Nuclei were collected by centrifugation at 1,000*g* for 5 min at 4 °C. The nuclear pellets were resuspended in ChIP buffer, followed by fragmentation using a Covaris E220 with the following settings: peak power, 140 W; duty factor, 5%; 200 cycles per burst, 4 °C for 900 s. Chromatin immunoprecipitation was performed using 4 µg of anti-RAD21 antibody (Abcam, ab992). Protein G agarose beads were used for pull-down of protein–DNA complexes. ChIP–seq library construction was performed using the Truseq ChIP Library Preparation Kit (IP-202–1012) according to the manufacturer's instructions. ChIP–seq libraries were quantified and sequenced using an Illumina NovaSeq 6000.

scRNA-seq

Lineage-depleted primary bone marrow precursors were electroporated with Cas9–crRNA–tracrRNA complexes containing NIPBL-crRNA1 and NIPBL-crRNA2. ATTO-550^{+} and ATTO-550^{-} cells were FACS sorted. Approximately 50,000 cells per sample were loaded into Single Cell A chips (10X Genomics) and partitioned into gel bead-in-emulsions (GEMs) in a Chromium Controller (10X Genomics). Single-cell RNA libraries were

prepared according to the 10X Genomics Chromium Next GEM Single Cell 3' HT Reagent Kits v.3.1 (Dual Index) User Guide and sequenced on a NovaSeq 6000.

Hi-C

Two independent replicates of ECOMG cells expressing the NIPBL-FKBP12^{F36V}-EYFP cassette were cultured with β-oestradiol and in the presence or absence of dTAG-13 for 72 h. Cells were cross-linked using formaldehyde. Cross-linked cells were processed for Hi-C using the Arima-HiC Kit (A510008) according to the manufacturer's instructions. The library preparation of Hi-C DNA was performed using the KAPA HyperPrep Kit (KK8502). The Hi-C libraries were sequenced with 150-bp paired-end reads (PE150) to a depth of approximately 600 million reads per sample on a NovaSeq 6000.

RNA-seq analysis

Quality control of the raw fastq files was performed using the software tool FastQC v.0.11.9 (ref. 46). Sequencing reads were aligned to the mouse genome (GRCm39.primary_assembly.genome.fa) using the STAR v.2.7.9a aligner[47]. Read quantification was performed with RSEM v.1.3.3 and Gencode annotation (gencode.vM27.primary_assembly. annotation.gtf). The R BioConductor package edgeR[48] was used to implement the limma-voom package for differential expression analysis. Genes expressed at low levels were filtered out (counts per million) > 1 for at least three samples). Trimmed mean of M-values (TMM) normalization was applied. The experimental design was modelled on treatment type, treatment, condition and time point (~0 +TreatmentType_Treatment_Condition_Timepoint). Significance was defined by using a P_{adj} cut-off of 0.05 after multiple testing correction using a moderated *t*-statistic in Limma. Functional enrichment of the differentially expressed genes was performed using GProfiler[49].

ATAC-seq analysis

Raw ATAC-seq data were processed with the ATAC-seq pipeline implemented in bcbio-nextgen v.1.2.8, which follows recommendations from the ENCODE ATAC-seq pipeline. Quality control of ATAC-seq data was performed using the software tools FastQC v.0.11.8, MultiQC v.1.10.1 and ataqv v.1.2.1. Raw reads were aligned to mm10 with BWA v.0.7.17 and duplicates, multimappers and reads aligning to mitochondria were removed. BAM files were then split into separate BAM files for the nucleosome free (NF), mononucleosome (MN), dinucleosome (DN) and trinucleosome (TN) fractions. Peaks were called with MACS2 v.2.2.7 (https://github.com/macs3-project/MACS) separately on each fraction and on all combined fractions. Consensus peaks of the nucleosome free peaks were created by taking the peak with the highest score when peaks overlap with bedops v.2.4.40. Peaks in Encode exclusion regions were removed (ENCFF547MET). We annotated peaks with the Bioconductor package ChIPseeker[50] and TxDb.Mmusculus.UCSC. mm10.knownGene. Functionalities of deeptools were used to analyse enrichment signals. *K*-means clustering (n = 2) was used to identify promoters and enhancer elements. Tornado plots were generated by 'computeMatrix' and 'plotHeatmap'. Summarized signal profiles were generated using 'plotProfile'. Quantification of signal strength was performed using PyRanges. Motif enrichment analysis was performed with Homer v.4.11 findMotifsGenome.pl -size given

for all differentially accessible peaks. Pile-ups were visualized using Integrative Genomics Viewer (IGV)[51].

Hi-C analysis

We used the runHiC pipeline (https://github.com/XiaoTaoWang/HiC_pipeline) to process Hi-C data. Specifically, we first used Chromap to map raw fastq files from Hi-C experiments to the mouse reference genome mm10 (ref. 52). We kept uniquely mapped reads, removed PCR duplicates and output the valid.pairs files defined by the 4DN consortium (https://github.com/4dn-dcic/pairix/blob/master/pairs_format_specification.md). In addition, to convert processed Hi-C data into the .hic format, for visualization we used the Juicer pipeline (https://www.aidenlab.org/juicebox/). We first performed this analysis for each biological replicate separately, and applied HiCrep to evaluate the reproducibility of Hi-C contact frequency between two biological replicates[53]. After confirming a high degree of reproducibility, we pooled the two biological replicates from the same experimental condition, and used the pooled Hi-C data for all of the downstream analysis. We plotted the average contact frequency as a function of genomic distance for all autosomes using 50 kbp bins. We performed A/B compartmentalization segregation analysis using at 50 kbp bin resolution intrachromosomal KR-normalized Hi-C contact matrices, after adjusting for 1D genomic distances. For each 50-kbp anchor bin, we calculated the average contact frequency between the anchor bin and other 50-kbp bins located in the same chromosome in the same compartment, as well as the average contact frequencies between the anchor bin and other 50-kbp bins in the same chromosome located in a different compartment. A/B compartment segregation scores for each 50 kbp bin were defined as the difference between the average contact frequency in the same compartment and the average contact frequency measured in different compartments. Finally, we used the HiCCUPS algorithm to identify at 10 kbp bin resolution chromatin loops for all autosomes using parameter settings as previously described[21]. We used HICCUPS to identify, at 10 kbp resolution, loops that spanned more than 5 Mb (mega-loops).

We applied a local background model similar to that described for the HiCCUPS algorithm to identify interchromosomal contacts that showed a significantly higher contact frequency when compared with their surrounding neighbourhood regions. Specifically, we first grouped at 50 kbp bin resolution interchromosomal Hi-C contact matrices into the unit of A/B compartment and used the A/B compartment resolution interchromosomal contacts for the downstream analysis. For each pair of compartments, termed as a point of interest (POI), we used interaction frequencies between the immediate upstream and downstream compartments as the local background control (CTL). Next, we calculated the sum of KR-normed interchromosomal Hi-C contact frequency in POI and CTL, respectively, and then derived the $\log_2$-transformed fold change between POI and CTL (termed as $\log_2$ FC). We found that the $\log_2$ FC has distinct distributions for A-A, B-B or A-B compartment resolution interchromosomal contacts. We then converted the $\log_2$ FC of A-A compartment resolution interchromosomal contact into *Z*-scores, and defined a pair of compartments as interchromosomal contact if $\log_2$ FC > 3.52 (that is, *Z*-score > 2.576 with two-sided $P = 0.01$), and average sum of KR-normalized interchromosomal Hi-C contact frequency per 1-Mb bin pairs > 100.

The proportions of interchromosomal contact were calculated as follows. Progenitor ECOMG cells that were cultured in the absence of dTAG-13 showed 1.025 billion intrachromosomal versus 102 million interchromosomal contacts, yielding a proportion of interchromosomal contacts of 9.0%. NIPBL-depleted cells that were cultured in the presence of dTAG-13 showed 1.086 billion intrachromosomal contacts versus 163 million interchromosomal contacts, yielding a proportion of 13.1%. To quantitatively assess how interchromosomal contact frequencies correlate with alterations in gene expression, we examined how interchromosomal contacts were related to significant changes in gene expression when compared with other euchromatic genomic regions with similar gene densities but did not show enrichment for interchromosomal contacts. Specifically, we segregated 9,655 genes whose transcription start sites were located in the euchromatic (A) compartment into two groups: 3,951 genes associated with interchromosomal contacts and 5,704 genes without interchromosomal contacts. To adjust for differences in gene density, we divided 9,655 genes into 3 groups on the basis of low, median and high gene density.

GO term enrichment analysis

We used the online software Enrichr (https://maayanlab.cloud/Enrichr/) with the default parameter setting for the gene set GO term enrichment analysis[54].

Transcription factor motif enrichment analysis

We used HOMER (http://homer.ucsd.edu/homer/) to perform the transcription factor motif enrichment analysis.

ChIP–seq analysis

ChIP–seq reads from ECOMG progenitors and ECOMG differentiated progeny, including H3K4me1, H3K4me3 and H3K27Ac, were described previously[24]. RAD21 ChIP–seq reads obtained for ECOMG progenitors and NIPBL-depleted ECOMG cells were analysed as follows. FASTQC v.0.12.1 was used to check the sequencing quality. A publicly available ChIP–seq data-analysis pipeline (https://hbctraining.github.io/Intro-to-ChIPseq-flipped/) was used to process the RAD21 ChIP–seq data. In brief, Bowtie2 v.2.5.1 was used to map the fastq files to the reference genome mm10 with the following parameters: bowtie2 -p 10 -q (query input files are FASTQ.fq/.fastq (default)) --local -x mm10(ReferenceGenome) -U Inputfastq -S SAMfile. Samtools v.1.17 was used to remove PCR duplicates. Only the uniquely mapped reads were included for further processing. MACS2 v.2.2.7.1 was used to call RAD21 ChIP–seq peaks with the following parameters: macs2 callpeak -t TAGbam -c Inputbam -f BAM -n NO.TAG --outdir outputdirectory -B. To ensure high data quality, we called RAD21 occupancy using an FDR < 1×10^{-25} and >5-fold enrichment. Using this approach, we identified 17,066 RAD21-bound sites in ECOMG progenitors and 8,304 RAD21-bound sites in NIPBL-depleted ECOMG progenitors.

scRNA-seq data analysis

CellRanger pipeline: we used CellRanger to process the raw Illumina NOVAseq sequencing files (CellRanger v.6.0.0, 10X Genomics). First, the CellRanger mkfastq pipeline was used to demultiplex each sequencing library by sample index to generate fastq files for paired-end

reads. The fastq files were then passed to the CellRanger Count pipeline, which used STAR aligner (STAR 2.7.2a) to align reads to the mouse reference genome (mm10)[47]. The Parameter –include-introns was used in the CellRanger Count pipeline. All subsequent data analysis was performed in R version 4.0.3. Seurat object filtration: filtering, normalization, scaling and clustering of data were performed using Seurat v.4.0.640 (ref. 55). The Seurat object was created with a min.cells of 2 and a min.features of 200. All cells expressing fewer than 200 or more than 6,000 genes or greater than 10% mitochondrial counts were removed to discard potential doublets and low-quality captures. Samples were merged using the Seurat merge function. Gene counts were log-normalized and 1,000 highly variable genes were selected on the basis of dispersion and mean expression. Scaled gene expression was calculated using Seurat's 'ScaleData' function, using the variable genes calculated before. Principal component analysis (PCA) was applied for dimension reduction and the 20 most informative principal components (PCs) were selected for clustering. We clustered cells according to graph-based methods (KNN and Louvain[56] community detection method) implemented in Seurat at a resolution of 0.6. Cluster cell type identification: cellular identity was determined by finding differentially expressed (DE) genes for each cluster using the Wilcoxon rank-sum test implemented in Seurat with a min.pct of 0.25 and a logfc.threshold of 0.25 (FindMarkers), and comparing those top expressing genes to known cell-type-specific genes from previous datasets.

Integration with public data

Raw count matrices were downloaded from GSM5029336 and GSM5029339 (ref. 25). The Seurat object was created with a min.cells of 1 and a min.features of 200. All cells expressing fewer than 200 or more than 3,000 genes or greater than 5% mitochondrial counts were removed to discard potential doublets and low-quality captures. For the GSM5029339 data, we adjusted the upper threshold for gene expression to keep all cells expressing more than 5,000 genes. Normalization and scaling were done as explained for our scRNA-seq data. We used the Anchor integration method from Seurat to integrate these datasets with our scRNA-seq data. We identified anchors using the FindIntegrationAnchors function, and used these anchors to integrate the datasets together with IntegrateData. The integrated assay was scaled, and 30 PCs were selected after PCA analysis. We then clustered cells according to graph-based methods (KNN and Louvain community detection method) implemented in Seurat at a resolution of 0.6. Known cell-type-specific genes were used to annotate the bone marrow cells. For visualization, 436 cells were removed from bone marrow data that were either mitochondrial enriched or for which no associated markers were found. To recover directed dynamic information for individual cells, we used the CellRank1 (ref. 57) Python package (v.1.5.0) to infer cell-state dynamics. CellRank uses a directed graph representation of the cells, in which the edges represent potential lineage relationships between the cells. To obtain a directed cell–cell transition matrix CellRank, we used a KNN graph and a pseudotime to bias the graph such that edges are likely to point in the direction of increasing pseudotime. To circumvent the need to define a root cell for pseudotime computation, CellRank uses the CytoTRACE score[58] to direct graph edges to point in the direction of increasing differentiation status. First, we applied the CytoTRACEKernel() function with default parameters to calculate the pseudotime. Then the transition matrix is generated using compute_transition_matrix(threshold_scheme = "soft",

nu = 0.5). This transition matrix was projected into the Seurat embedding to draw the arrows like velocity plots (compute_projection(basis = “force_directed”)).

Extended Data

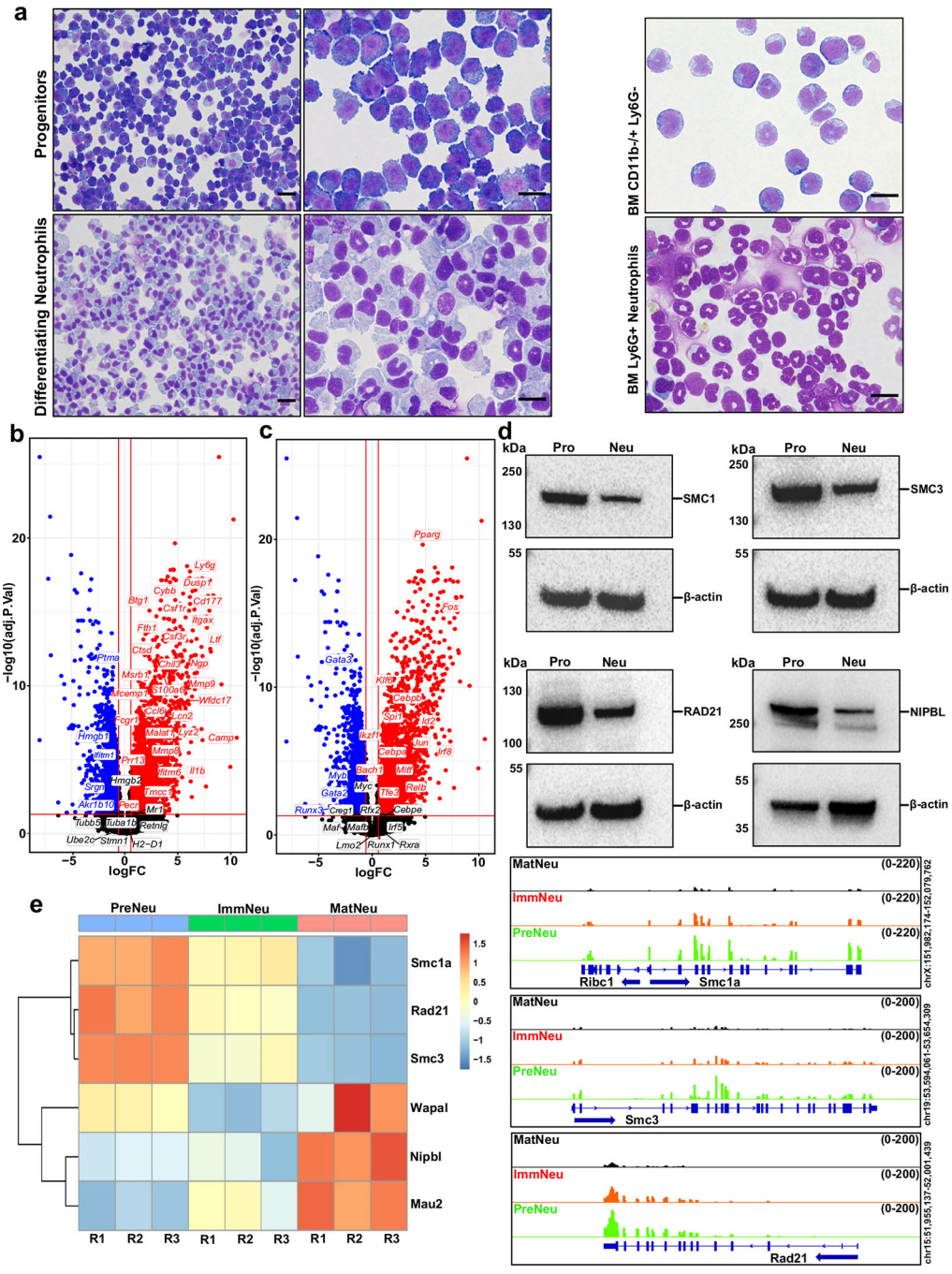

Extended Data Fig. 1 |. Declines in SMC1, SMC3a and RAD21 expression in differentiating neutrophils.

a, Left images represent Wright–Giemsa staining of ECOMG progenitors cultured in the presence (top images) or absence (bottom images) of β-oestradiol (n = 500 cells). Scale

bars, 20 μm (left image) and 10 μm (right image). Right images represent Wright–Giemsa staining of $CD11b^{-/+}Ly6G^{-}$ neutrophil progenitors (upper image) and $CD11b^{+}Ly6G^{+}$ differentiated neutrophils (lower image) isolated from the bone marrow. Scale bars, 10 μm. **b**, Volcano plot shows relative transcript abundance in ECOMG progenitors cultured in the absence versus presence of β-oestradiol. Upregulated transcripts are shown in red while downregulated transcripts are indicated in blue. Genes closely associated with a neutrophil-specific gene program are highlighted. **c**, Volcano plot highlights transcripts encoding for transcription factors that instruct neutrophil cell fate. Volcano plots represent the results of the limma-voom differential expression analysis displayed as the log2 fold change by the −log10 of the adjusted *P* value of each gene. Upregulated genes defined $P_{adj} < 0.05$ and $\log_2$-transformed fold change > 1 are represented in red. Downregulated genes defined as $P_{adj} < 0.05$ and $\log_2$-transformed fold change < −1 are represented in blue. **d**, Western blot analysis of SMC1a, SMC3, RAD21 and NIPBL protein levels in ECOMG progenitors and differentiated neutrophils are shown. **e**, Heat map indicating normalized transcript counts (DESeq2) and the genome browser tracks (IGV) of RNA-seq indicating transcript abundance for factors that instruct loop extrusion in neutrophil progenitors and differentiated neutrophils derived from mouse bone marrow are shown.

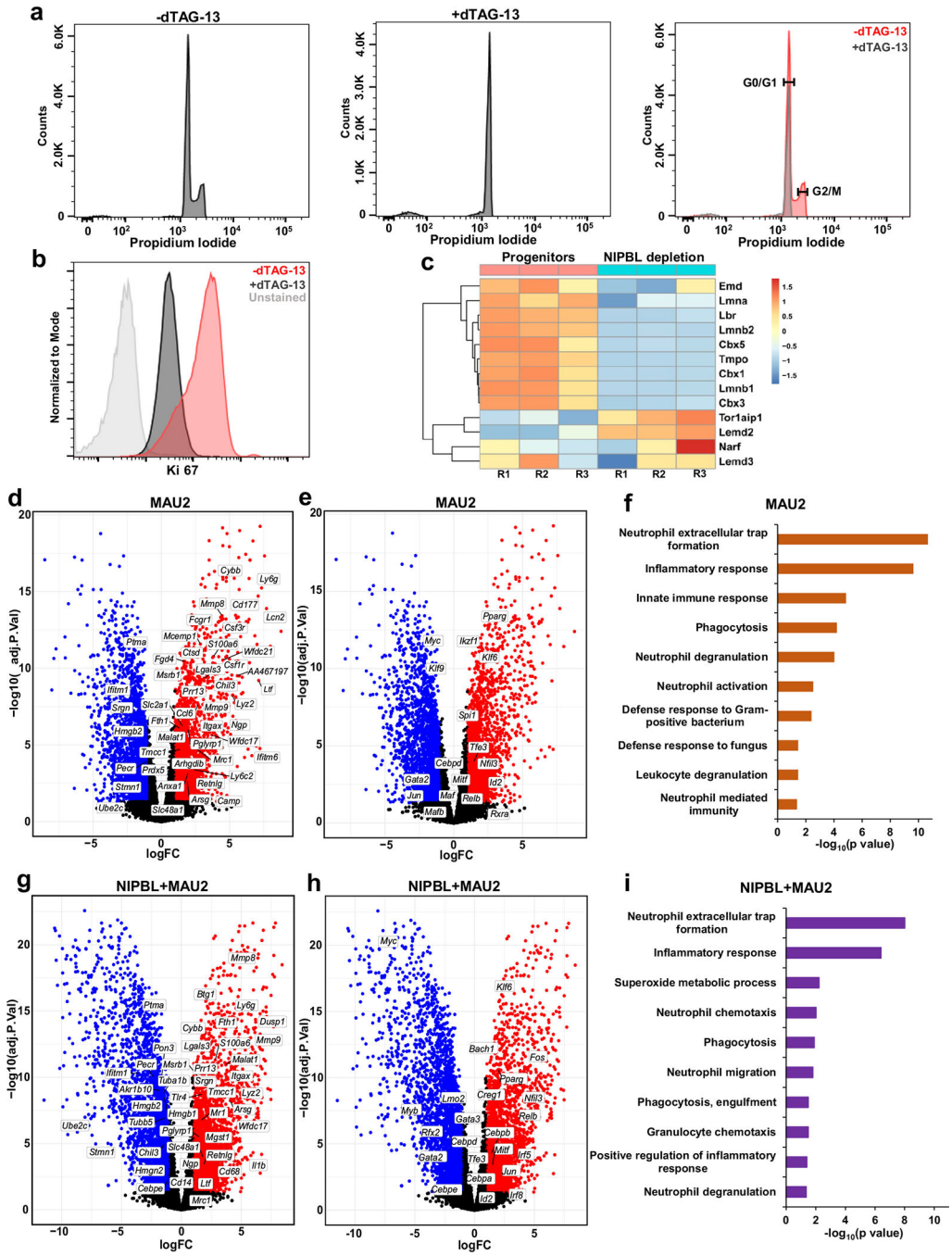

Extended Data Fig. 2 |. Depletion of the loop-extrusion loading factors NIPBL and MAU2 instructs cell-cycle arrest and orchestrates distinct neutrophil-specific gene programs.

a, Flow cytometry analyses of propidium iodide staining for NIPBL-FKBP12^{F36V}-EYFP ECOMG cells cultured for 72 h in the absence or presence of dTAG-13 are shown. **b**, Intracellular staining of the proliferation marker Ki-67 in NIPBL-FKBP12^{F36V}-EYFP cells cultured for 72 h in the absence or presence of dTAG-13 is shown. **c**, Heat map indicating mRNA abundance encoding for factors involved in structuring the nuclear envelope in ECOMG progenitors and NIPBL-depleted ECOMG progenitors. **d**, Volcano plot

represents the differential expression of transcripts in ECOMG progenitors carrying MAU2-FKBP12^{F36V}-mScarlett cassettes were cultured for 72 h with β-oestradiol in the absence or presence of dTAG-13. Upregulated genes defined by $P_{adj} < 0.05$ and $\log_2$-transformed fold change > 1 are represented in red. Downregulated genes defined by $P_{adj} < 0.05$ and $\log_2$-transformed fold change < −1 are represented in blue. **e**, Depletion of MAU2 activates the expression of genes encoding for transcription factors that instruct neutrophil cell fate. **f**, GO-based functional classification of differentially expressed transcripts in MAU2-depleted cells. Representative pathways that relate to neutrophil differentiation and inflammation are shown. **g**, Depletion of both NIPBL plus MAU2 activates a neutrophil-specific transcription signature. Volcano plot shows differential transcript levels in ECOMG progenitors carrying both NIPBL-FKBP12^{F36V}-EYFP and MAU2-FKBP12^{F36V}-mScarlet cassettes that were cultured for 72 h with β-oestradiol and in the absence or presence of dTAG-13. Genes closely associated with a neutrophil-specific gene program are highlighted. Upregulated genes defined as $P_{adj} < 0.05$ and $\log_2$-transformed fold change > 1 are represented in red. Downregulated genes defined as $P_{adj} < 0.05$ and $\log_2$-transformed fold change < −1 are represented in blue. **h**. Volcano plot highlights transcripts encoding for neutrophil-signature transcription factors. **i**, GO-based functional classification of differentially expressed transcripts in cells depleted for both NIPBL and MAU2. Representative pathways that relate to neutrophil differentiation and inflammation are shown.

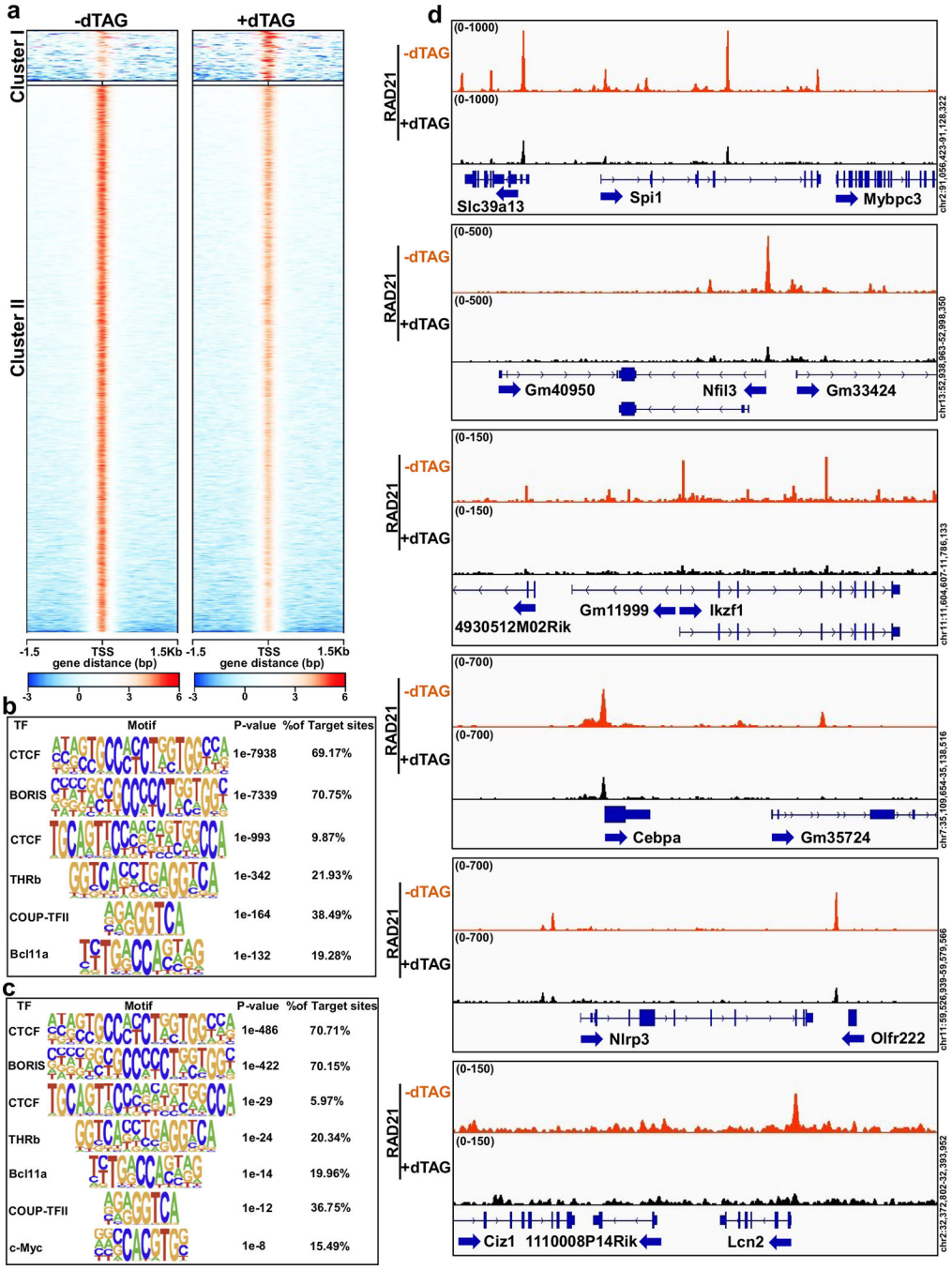

Extended Data Fig. 3 |. Depletion of NIPBL interferes with RAD21 occupancy.

a, NIPBL depletion modulates Rad21 occupancy. NIPBL-FKBP12^{F36V}-EYFP progenitors were cultured with β-oestradiol in the absence or presence of dTAG-13. RAD21 occupancy was analysed using ChIP–seq analysis and presented as tornado plots. Cluster I is comprised of RAD21-binding sites that were enriched upon depletion of NIPBL. Cluster II consists of RAD21-binding sites that were depleted upon removal of NIPBL. In NIPBL-depleted cells 9,293 RAD21-binding sites were lost, 531 binding sites were gained and 7,773 binding sites were shared. RAD21 peaks were generated using FDR <1e-25 and fold enrichment >

5. **b**, *Cis* elements associated with 9,293 RAD21-bound sites that were depleted in NIPBL-depleted cells. *P* values for motif enrichment and matched transcription-factor-binding sites are indicated. **c**, *Cis* elements associated with 531 RAD21-bound sites that were gained upon removal of NIPBL expression. **d**, Genome browser tracks represent ChIP–seq reads in ECOMG progenitors cultured in the absence or presence of dTAG-13. IGV Tracks for Spi1, Nfil3, Ikzf1, Cebpa, Nlrp3 and Lcn2 loci are shown.

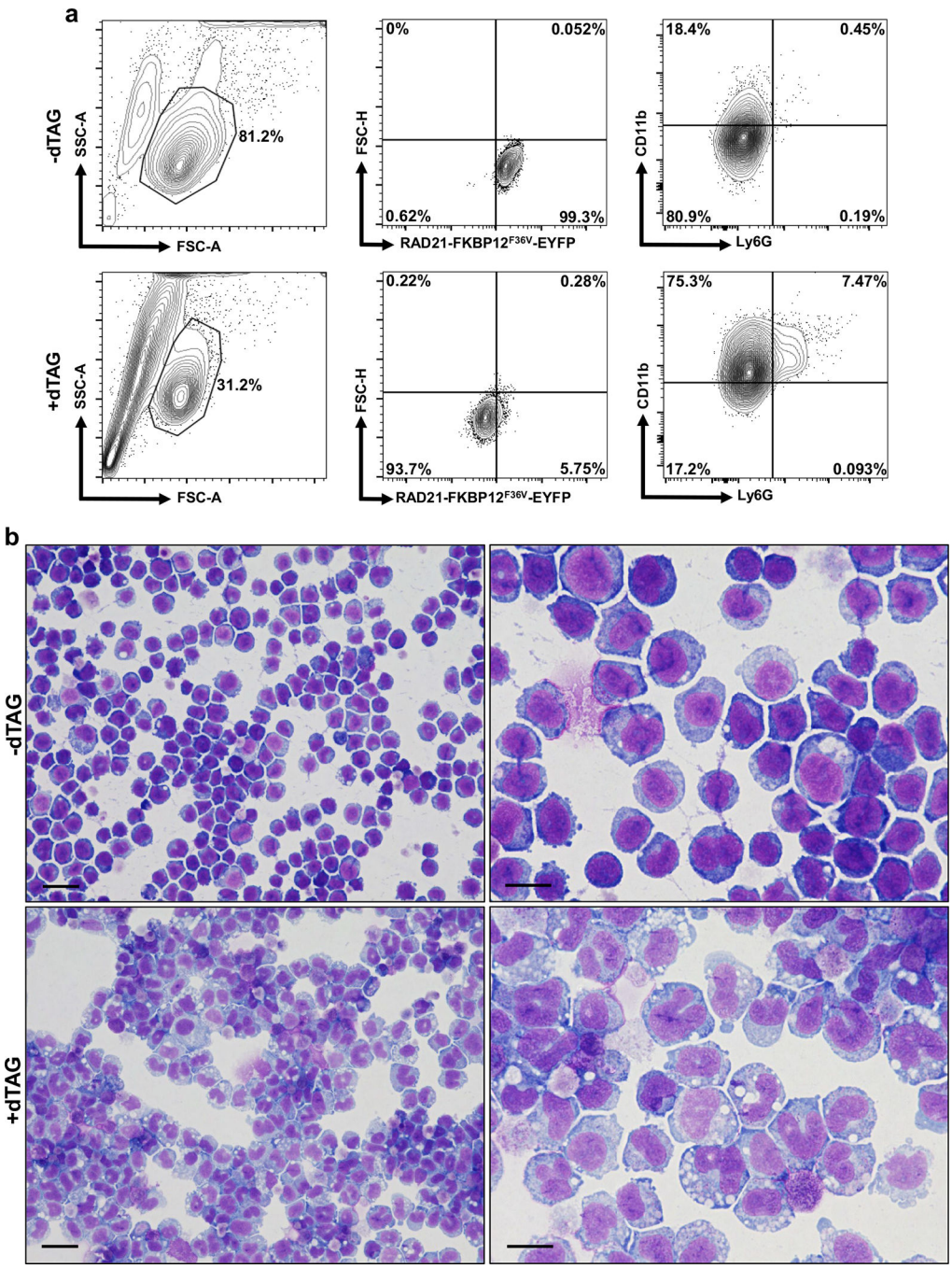

Extended Data Fig. 4 |. Depletion of RAD21 instructs the assembly of polymorphonuclear structures.

a, ECOMG cells carrying RAD21-FKBP12^{F36V}-EYFP cassettes integrated into the endogenous RAD21 loci were cultured for 36 h with β-oestradiol in the absence or presence of dTAG-13. Flow cytometry analysis shows gating of live cells using FSC-A and SSC-A. Gated, live single cells were used for the analysis of EYFP, CD11b and Ly6G expression. **b**, Wright–Giemsa staining of RAD21-FKBP12^{F36V}-EYFP ECOMG cells cultured with β-oestradiol alone (top images) or in the presence of both β-oestradiol and dTAG-13 (bottom images). Objectives used were 40× (left) and 100× (right). Scale bars, 20 μm (left) and 10 μm (right).

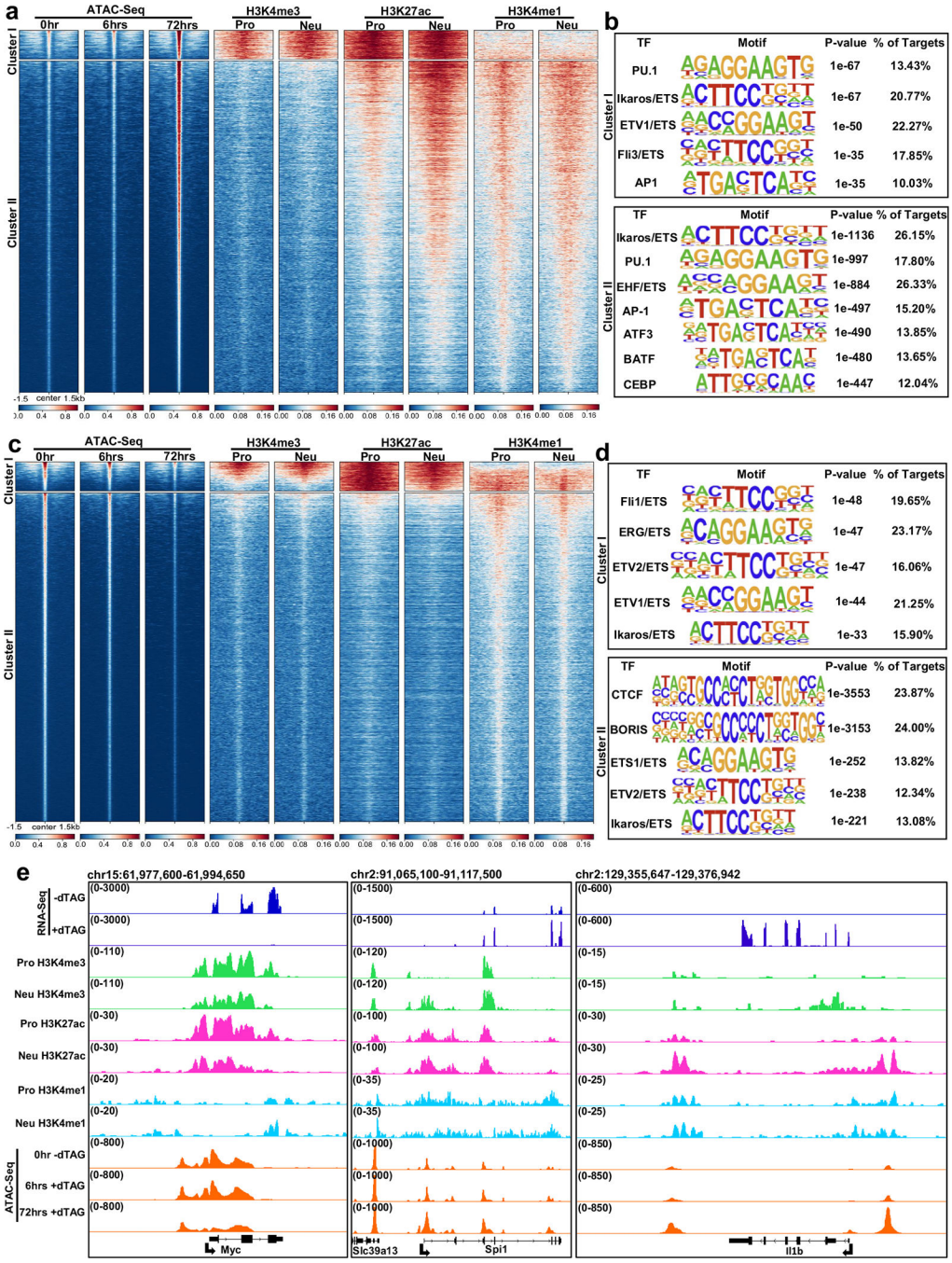

Extended Data Fig. 5 |. Depletion of NIPBL increases chromatin accessibility at neutrophil-specific promoters and enhancers.

a, NIPBL depletion increases chromatin accessibility across enhancer and promoter elements. NIPBL-FKBP12^{F36V}-EYFP ECOMG progenitors were cultured with β-oestradiol in the absence or presence of dTAG-13. Changes in chromatin accessibility of cells cultured in the absence (0 h) or presence of dTAG-13 (6 and 72 h) were analysed and presented as tornado plots. Clusters were generated using K-means clustering (n = 2). The number of regions associated with neutrophil-specific promoters (H3K4me3), active enhancers (H3K27Ac and H3K4me1) or weak enhancers (H3K4me1) and transcriptionally silent

regions are shown. Tornado plots were generated by sorting maximum signal strength intensities for ATAC-seq reads. Colour scale intensities represent normalized read scores (reads per 10 million uniquely mapped reads per base pair). **b**, *Cis* elements associated with increased chromatin accessibility at enhancers and promoters are shown. *P* values for motif enrichment and matched transcription-factor-binding sites are indicated. **c**, NIPBL depletion decreases chromatin accessibility across a subset of enhancer and promoter elements. Changes in chromatin accessibility of cells cultured in the absence (0 h) or presence of dTAG-13 (6 and 72 h) were analysed and presented as tornado plots. **d**, *Cis* elements associated with decreased chromatin accessibility at enhancers and promoters are shown. **e**, Genome browser tracks depicting RNA-seq, ChIP–seq and ATAC-seq reads at the *Myc*, *Spi1* and *Il1b* loci are shown.

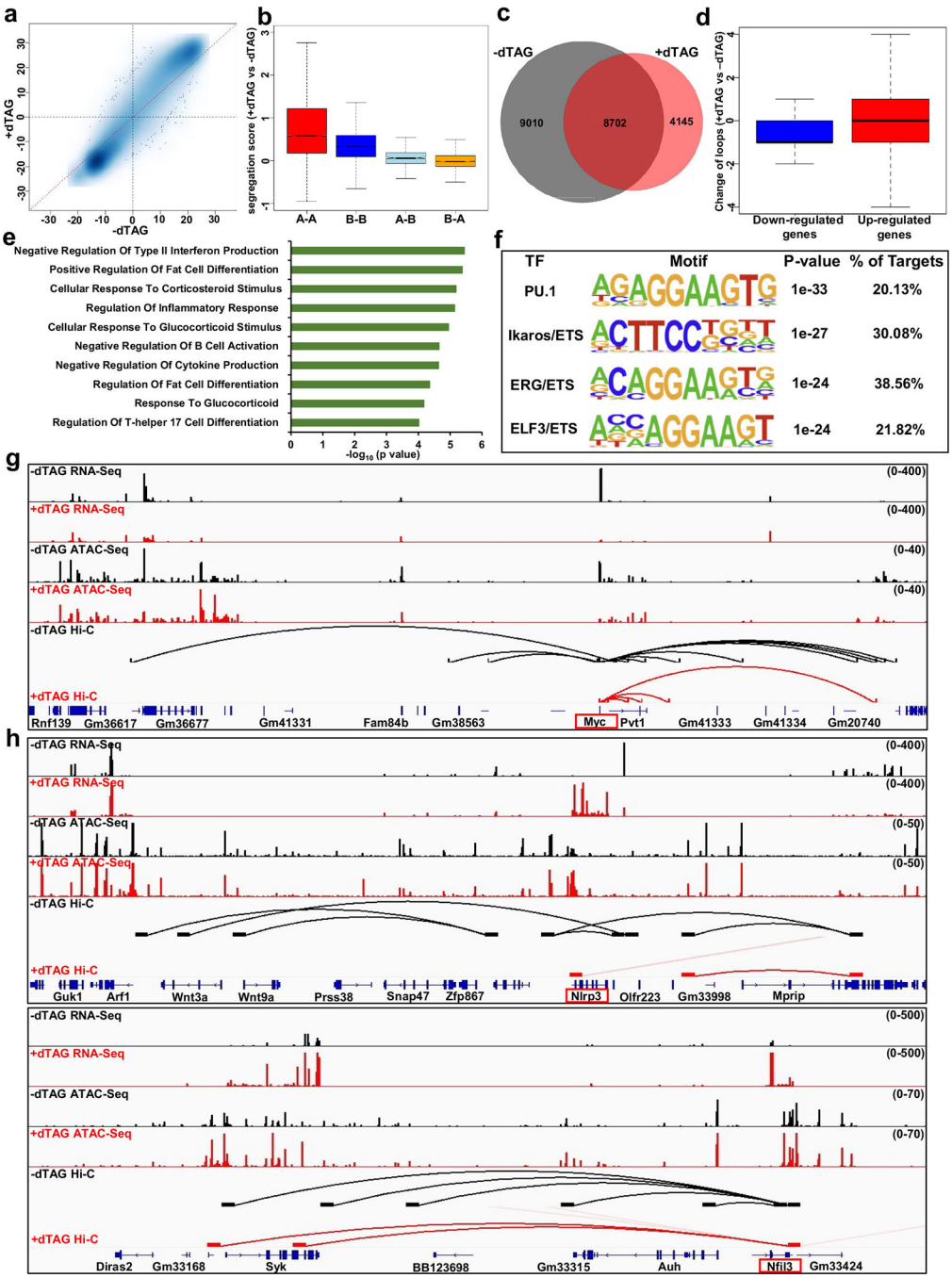

Extended Data Fig. 6 |. Halting loop extrusion leads to widespread changes in chromatin folding to orchestrate an inflammatory gene program.

a, Scatter plot shows A versus B compartmentalization (50 kbp resolution) in NIPBL-FKBP12^{F36V}-EYFP ECOMG cells cultured in the absence (x axis) or presence of dTAG-13 (y axis). **b**, Box plot represents differential segregation scores (50 kbp resolution) for cells cultured in the absence versus presence of dTAG-13. one-sided $P < 0.05$. In each box, the upper edge, horizontal centre line and lower edge represent the 75th percentile, median and 25th percentile, respectively. The upper whiskers represent the 75th percentile + 1.5× the

IQR. The lower whiskers represent the 25th percentile - 1.5× the IQR. **c**, Venn diagram indicates number of gained or lost chromatin loops in NIPBL-FKBP12^{F36V}-EYFP ECOMG cultured in the absence versus presence of dTAG-13. **d**, Transcript abundance correlates with the assembly of loops in NIPBL-FKBP12^{F36V}-EYFP cells cultured in the absence versus the presence of dTAG-13. Mean change and corresponding distribution of loops associated with transcriptional silencing or activation log2 FC > = 2 or log2 FC < = −2) in NIPBL-depleted cells are shown. **e**, GO-based functional classification of differentially expressed transcripts that are associated with gained paired promoter and enhancer elements in NIPBL-depleted cells. **f**, *Cis* elements associated with increased chromatin accessibility at enhancers and promoters are shown. *P* values for motif enrichment and matched transcription-factor-binding sites are indicated. **g**, Genome browser tracks indicate RNA-seq, ATAC-seq and Hi-C reads across the *Myc* locus for NIPBL-FKBP12^{F36V}-EYFP ECOMG cells cultured in the absence or presence of dTAG-13. **h**, Genome browser tracks indicate RNA-seq, ATAC-seq and Hi-C reads across the *Nlrp3* and *Nfil3* loci for NIPBL-FKBP12^{F36V}-EYFP cells cultured in the absence or presence of dTAG-13.

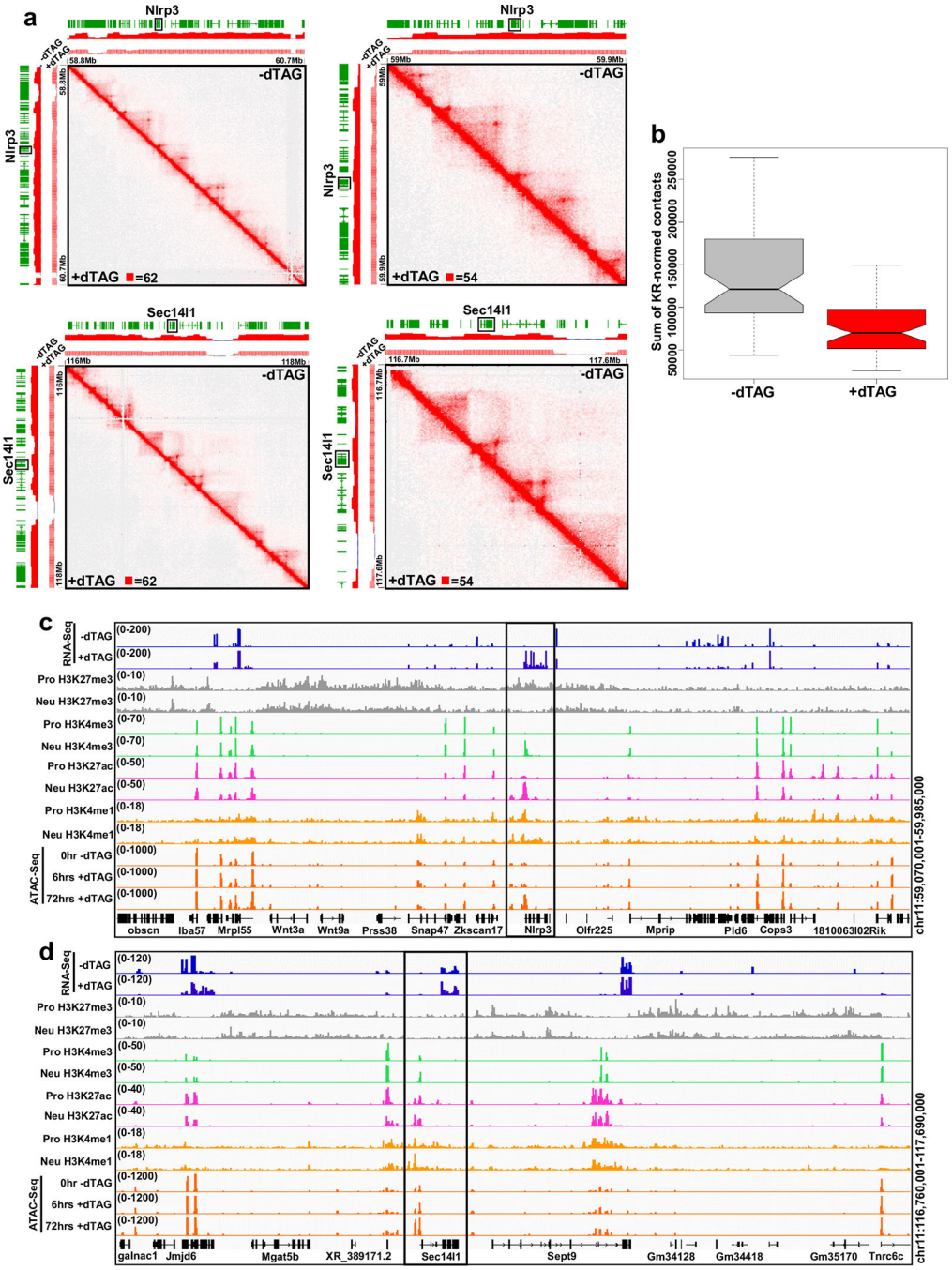

Extended Data Fig. 7 |. Structure of a mega-loop body pairing the *NLRP3* and *SEC14l1* loci into a common hub.

a, Ten kb resolution (left) and 5 kbp resolution (right) KR-normalized Hi-C contact matrices indicating loop bodies that span *Nlrp3* and *Sec14l1* loci across chromosome 11 are shown in ECOMG progenitors (−dTAG−13) and NIPBL-depleted cells (+dTAG-13). **b**, Box plot shows the sum of KR-normalized-interaction frequencies across a gained mega-loop body spanning the *Nlrp3* and *Sec14l1* loci in ECOMG progenitors (−dTAG) and NIPBL-depleted cells (+dTAG). Two-sided two-sample T-test was performed. $P = 1.72 \times 10^{-9}$. In each box,

the upper edge, horizontal centre line and lower edge represent the 75th percentile, median and 25th percentile, respectively. The upper whiskers represent the 75th percentile + 1.5× the IQR. The lower whiskers represent the 25th percentile − 1.5× the IQR. **c**,**d**, Genome browser tracks depicting RNA-seq, ChIP–seq and ATAC-seq reads at mega-loop interactions involving the *Nlrp3* **(c)** and *Sec14l1* **(d)** loci in cells cultured with β-oestradiol and in the absence or presence of dTAG-13. Note that ChIP–seq reads were derived from ECOMG cells cultured in the presence of β-oestradiol (Pro) versus absence of β-oestradiol (Neu)[24].

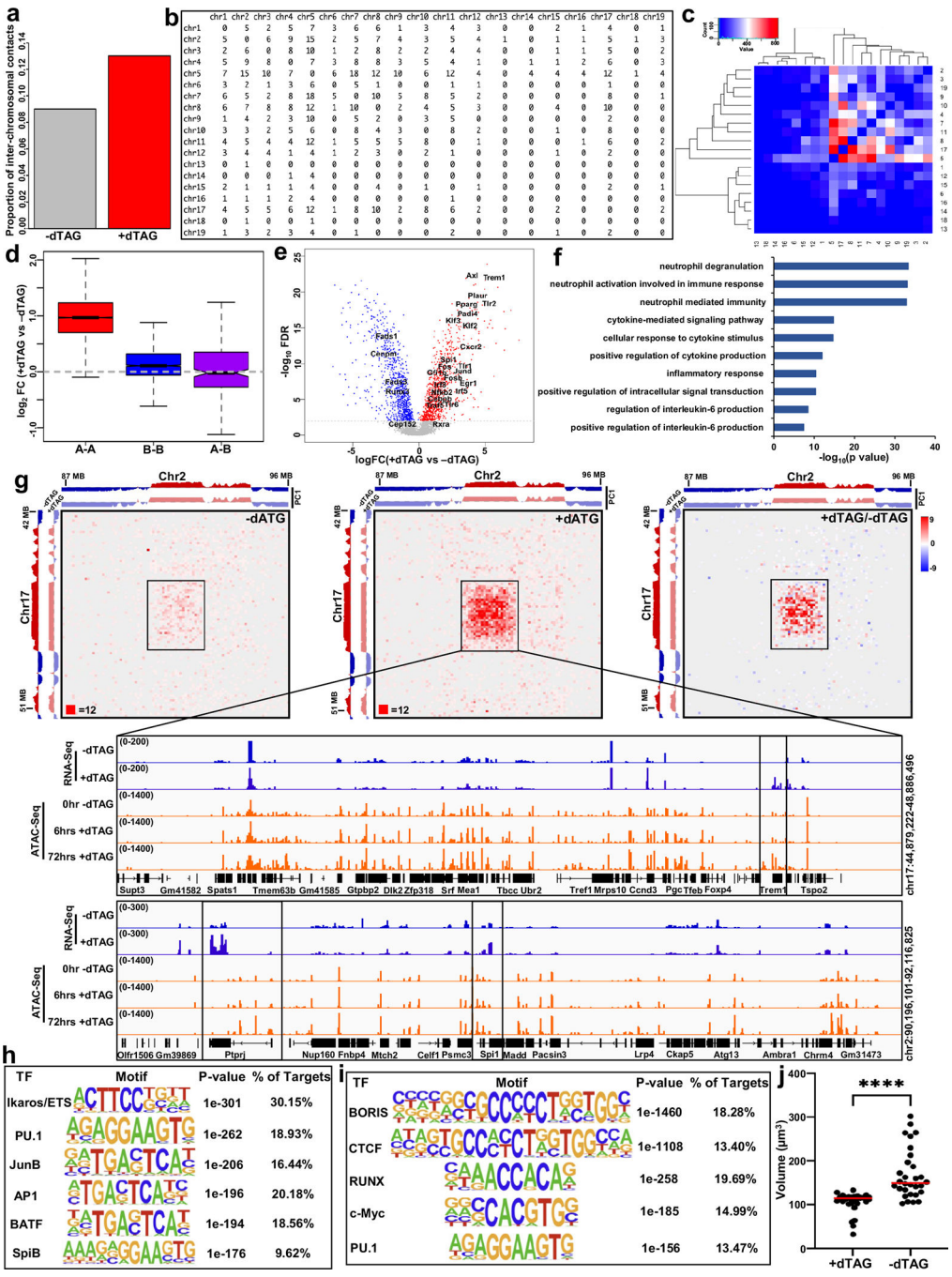

Extended Data Fig. 8 |. Halting loop extrusion enriches for interchromosomal interactions and reduces nuclear volume.

a, Proportions of interchromosomal contacts detected for NIPBL-FKBP12^{F36V}-EYFP cells cultured in the presence versus absence of dTAG-13 are shown (see Methods). **b**, Table depicts the frequency of interchromosomal interactions enriched in NIPBL-depleted cells. Log2 FC > 3.52 (Z-score > 2.576 with two-sided $P = 0.01$). **c**, Heat map shows clustering of interacting chromosomes normalized for size. **d**, Log2 fold change of transcripts abundance associated with A-A, B-B and A-B compartmental domains at interchromosomal interaction hubs in NIPBL-depleted cells. Z-score>1.96. In each box, the upper edge, horizontal centre line and lower edge represent the 75th percentile, median and 25th percentile, respectively. The upper whiskers represent the 75th percentile + 1.5× the IQR. The lower whiskers represent the 25th percentile - 1.5× the IQR. **e**, Volcano plot shows the differential expression of 3,951 genes located at interchromosomal hubs that were enriched in NIPBL-FKBP12^{F36V}-EYFP cells cultured in the presence versus absence of dTAG-13. **f**, GO enrichment analysis for genes located at interchromosomal contact hubs that were enriched in NIPBL-FKBP12^{F36V}-EYFP cells cultured in the presence versus absence of dTAG-13. **g**, Heat maps show KR-normalized interchromosomal interactions (100 kbp resolution) involving chromosomes 2 and 17 for indicated cell types and culture conditions. Bottom, genome browser (IGV) tracks depicting RNA-seq and ATAC-seq reads at genomic regions of interchromosomal hubs involving chromosomes 2 and 17. **h**,**i**, Transcription factor motif analysis of gained (**h**) and lost (**i**) ATAC-seq peaks associated with gained interchromosomal interaction hubs enriched in NIPBL-depleted cells. **j**, Depletion of NIPBL reduces nuclear volume in ECOMG progenitors. Plots show nuclear volumes (μm^3) measured for NIPBL-FKBP12^{F36V}-EYFP cells cultured in the presence (n = 33 cells) versus absence (n = 30 cells) of dTAG-13. Unpaired *t*-test was performed (P < 0.0001).

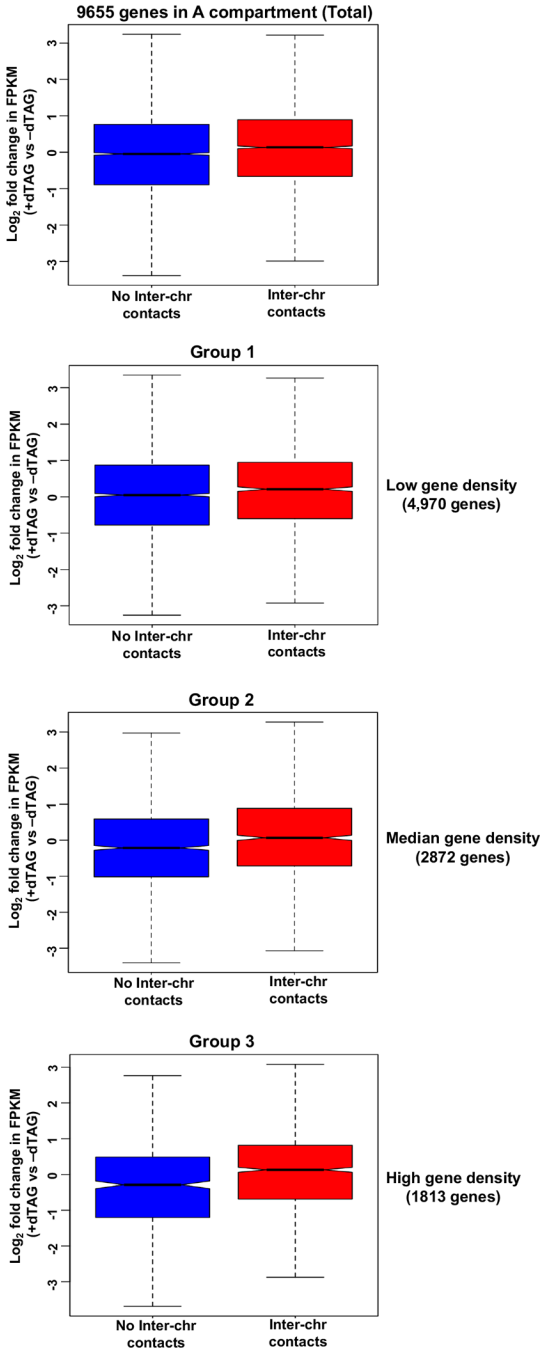

Extended Data Fig. 9 |. Halting loop extrusion activates gene expression at genomic regions enriched for interchromosomal interactions.

Box plots show log_2-transformed fold changes in FKPM reads (+dTAG versus −dTAG treated cells). In each box, the upper edge, horizontal centre line and lower edge represent the 75th percentile, median and 25th percentile, respectively. The upper whiskers represent the 75th percentile + 1.5× the IQR. The lower whiskers represent the 25th percentile − 1.5× the IQR. Genes whose transcription start sites were located in the euchromatic (A) compartment were segregated into 3 groups based on low, median and high gene density. At similar gene density, the euchromatic regions that were enriched for interchromosomal

interactions were associated with upregulated gene expression compared to the euchromatic regions without interchromosomal interactions. Two-sample *t*-test was performed. $P = 2.90 \times 10^{-9}$ (Total), $P = 0.0014$ (Group 1), $P = 1.83 \times 10^{-6}$ (Group 2), $P = 5.18 \times 10^{-10}$ (Group 3).

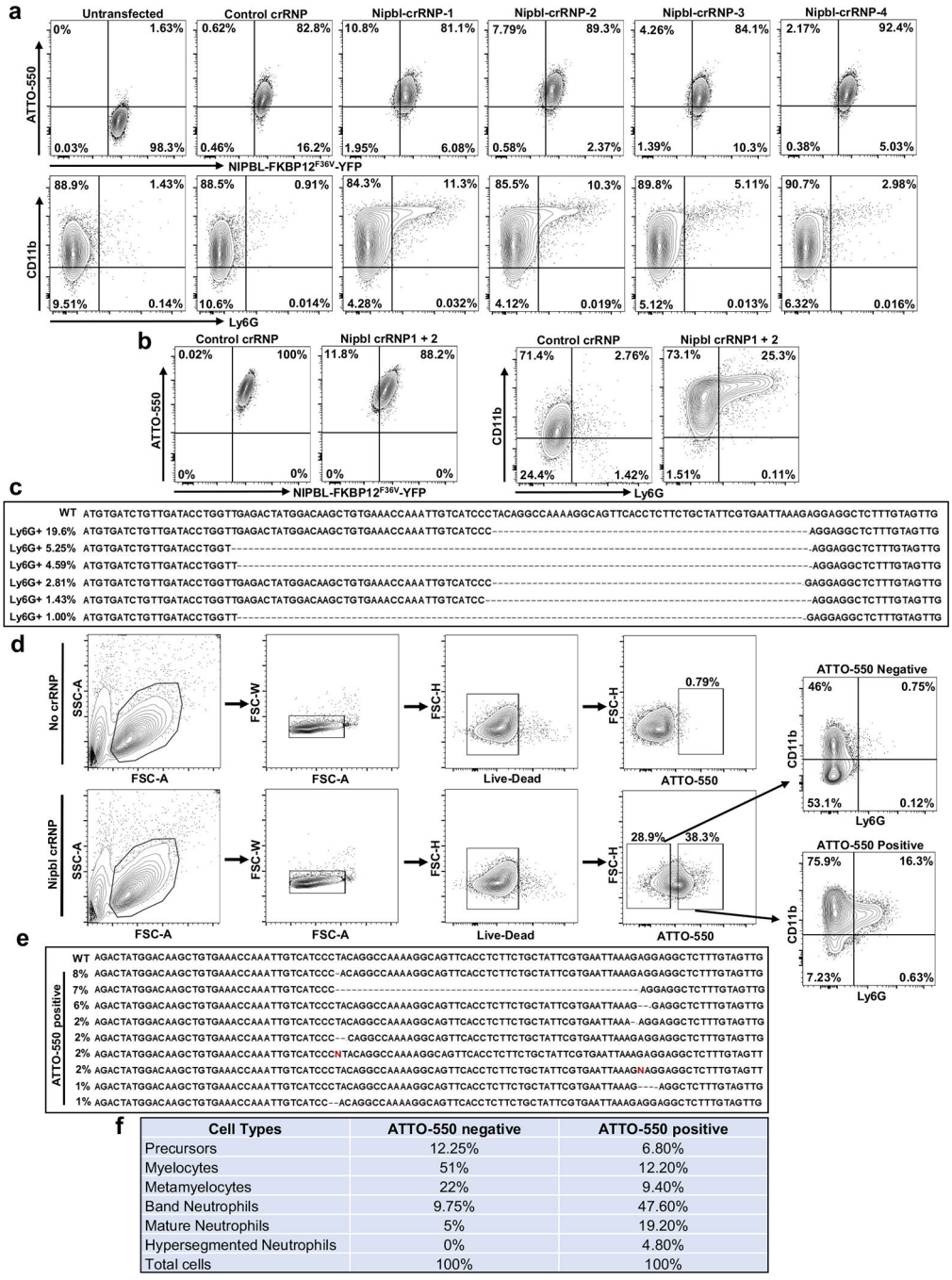

Cell Types	ATTO-550 negative	ATTO-550 positive
Precursors	12.25%	6.80%
Myelocytes	51%	12.20%
Metamyelocytes	22%	9.40%
Band Neutrophils	9.75%	47.60%
Mature Neutrophils	5%	19.20%
Hypersegmented Neutrophils	0%	4.80%
Total cells	100%	100%

Extended Data Fig. 10 |. Depletion of NIPBL in primary bone marrow haematopoietic progenitors enriches for polymorphonuclear cells.

a, NIPBL-FKBP12^{F36V}-EYFP ECOMG progenitors were electroporated with crRNAs that target four different genomic regions in NIPBL, named NIPBL-crRNA1–4, tracrRNAs

conjugated with ATTO-550 and Cas9. Electroporated ECOMG progenitors were cultured for three days in the presence of β-oestradiol and examined for CD11b and Ly6G expression. Upper panels show transfection efficiencies as reflected by ATTO-550 expression. ECOMG cells that were not electroporated served as a control. As an additional control ECOMG cells were electroporated with negative crRNPs (control RNPs) lacking specificity for genomic sequences (IDT). **b**, ECOMG cells electroporated with NIPBL-crRNPs 1 + 2 and control crRNPs were analysed for the expression of CD11b and Ly6G. **c**, ECOMG cells were electroporated with NIPBL-crRNPs 1 + 2. Ly6G+ cells were sorted after 72 hrs. Sorted samples were examined by DNA sequencing for the presence of indels. **d**, Lin- primary bone marrow progenitors were electroporated with crRNPs 1 + 2 targeting NIPBL. Electroporated cells were cultured for three days in the presence of SCF and Flt3L and examined for transfection efficiencies and for CD11b and Ly6G expression. **e**, Three days after electroporation ATTO-550^{-} and ATTO-550^{+} cells were sorted and analysed for the presence of indels. **f**, ATTO-550^{-} and ATTO-550^{+} cells were sorted and analysed for nuclear morphology using Wright–Giemsa staining. Table indicates the percentages of progenitors and differentiated progeny in cells transfected with crRNPs (1 + 2) that target NIPBL. A total of 400–500 cells for each condition was examined. All experiments were performed independently at least three times.

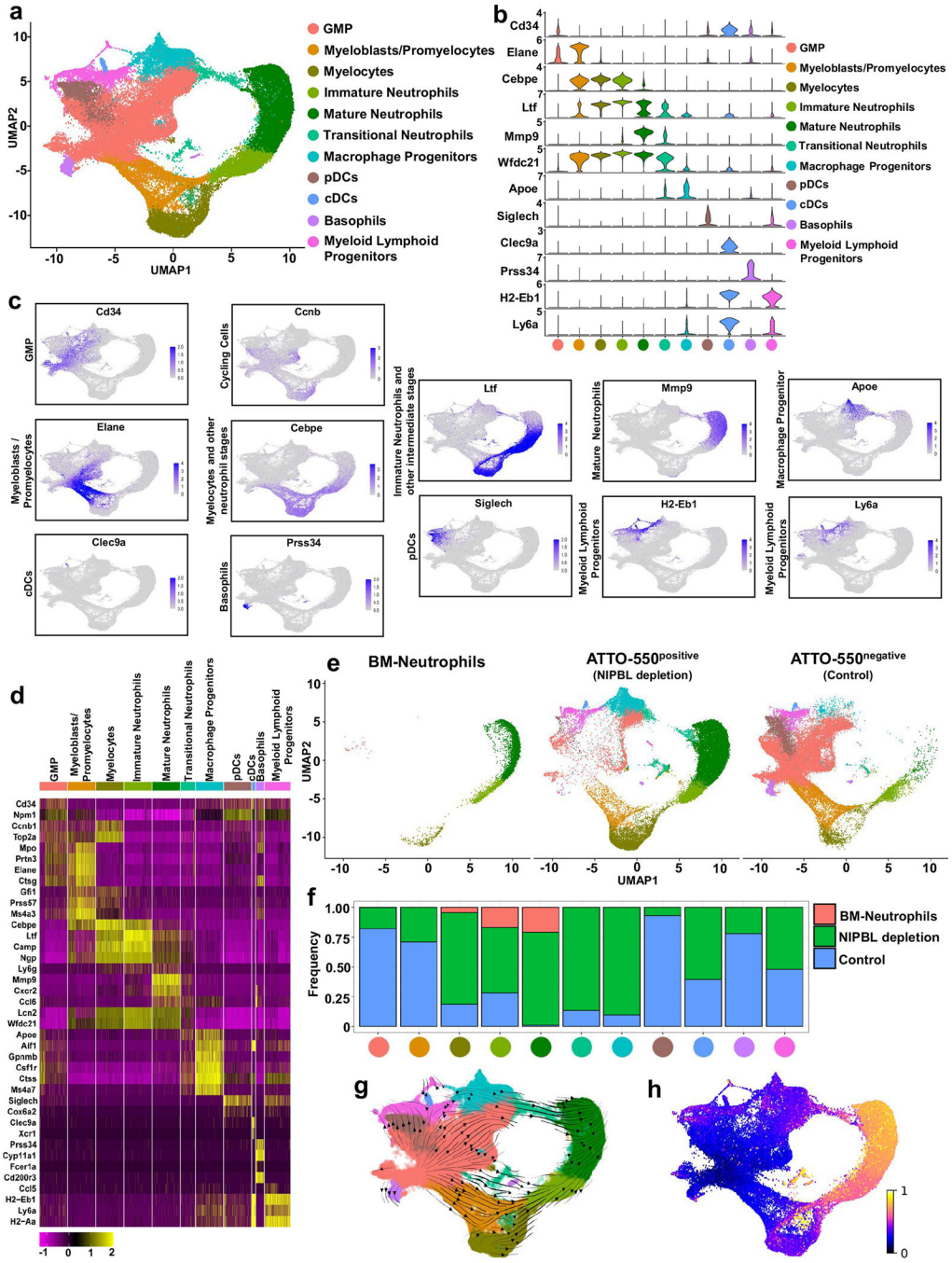

Extended Data Fig. 11 |. Depletion of NIPBL in primary bone marrow haematopoietic progenitors instructs the onset of neutrophil development.

a, UMAP plot derived from two independent replicates of ATTO-550^{-} (control) and ATTO-550^{+} (NIPBL-depleted) populations is shown. Different clusters representing hematopoietic populations are shown for GMPs, myeloblasts/promyelocytes, myelocytes, immature neutrophils, mature neutrophils, transitional neutrophils, macrophage progenitors, pDCs, cDCs, basophils and myeloid/lymphoid progenitors. **b**, Violin plots show the expression levels of cluster-specific transcripts. **c**, UMAP plots of cluster-specific transcript

distribution among GMPs, cycling cells, myeloblasts/promyelocytes, myelocytes, immature neutrophils, mature neutrophils, transitional neutrophils, macrophage progenitors, pDCs, cDCs, basophils and myeloid/lymphoid progenitors are shown. **d**, Heat map indicating cell-type specific expression of a selected group of transcripts. Cluster-specific differentially expressed genes were identified using Wilcoxon rank-sum test implemented in Seurat min.pct of 0.25 and a logfc.threshold of 0.25 (FindMarkers). **e**, UMAP plots were derived by integrating and clustering of scRNA-seq reads from bone-marrow-derived mouse neutrophils[25], ATTO-550^{-} (control) and ATTO-550^{+} (NIPBL-depleted) populations. **f**, The proportion of indicated cell types in ATTO-550^{-} (control) and ATTO-550^{+} (NIPBL-depleted) populations is shown. **g**, Cellular dynamics analysis indicates developmental trajectories adopted by differentiating neutrophils. Putative differentiation trajectories are shown. **h**, Pseudotime visualization of neutrophil differentiation instructed by NIPBL depletion in primary hematopoietic progenitors is shown. scRNA-seq data were generated from two independent biological replicates.

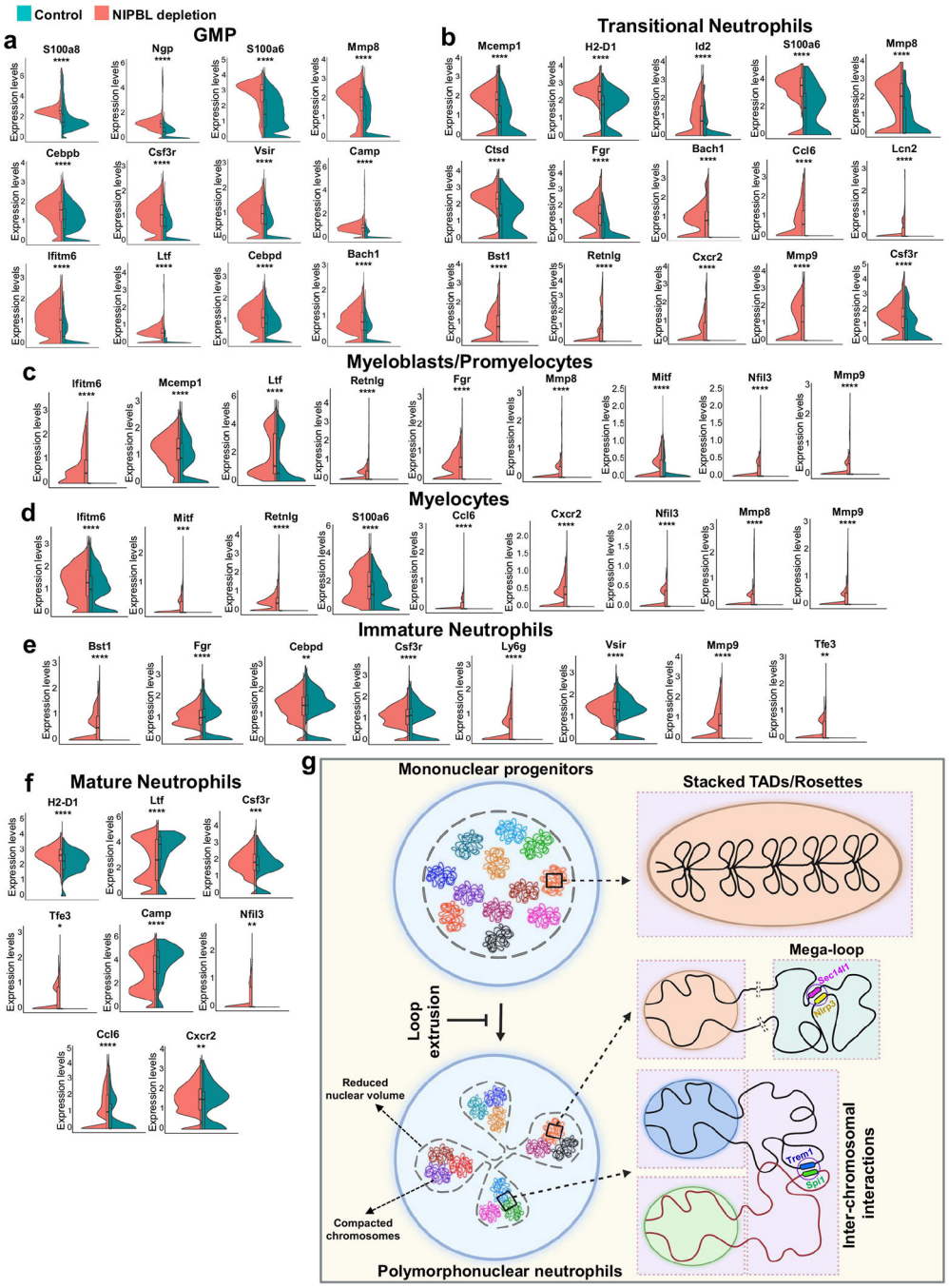

Extended Data Fig. 12 |. Depletion of NIPBL initiates a neutrophil-specific gene program in myeloid progenitors.

a–**f**, Violin plots indicate the expression patterns of neutrophil-signature genes in GMPs (**a**), transitional neutrophils (**b**), myeloblasts/promyelocytes (**c**), myelocytes (**d**), immature neutrophils (**e**) and mature neutrophils (**f**) derived from ATTO-550^{-} (control) and ATTO-550^{+} (NIPBL-depleted) populations. (*t*-test; ns: p > 0.05, *: p <= 0.05, **: p <= 0.01, ***: p <= 0.001, ****: p <= 0.0001). **g**, Model depicting the role of loop extrusion in mononuclear versus polymorphonuclear cell differentiation. Loop extrusion enforces

the checkpoint that orchestrates mononuclear versus polymorphonuclear cell fate choice. Chromosomes in mononuclear cells are shown as rigid chromatin fibres (stacked rosettes)[18]. In polymorphonuclear cells, chromosomes are depleted for rosettes to adopt flexible conformations that enable the assembly of mega-loops and interchromosomal interactions. Illustration was created using BioRender.

Supplementary Material

Refer to Web version on PubMed Central for supplementary material.

Acknowledgements

C.M. was supported by NSF-BSF2019280, NIH DK107977, NIH AI102853 and BIOREMC. Microscopy was supported by funds from the NIH (S10 OD030417) and an Imaging Scientist Grant from the Chan Zuckerberg Initiative (2019–198153). DNA sequencing was supported by funding from the NIH (S10 OD026929). M.H. was funded by funds from the NIH, including R35HG011922 and UM1HG011585. C.S.C. was supported by funds from the NIH, including R56AG074591, U01DA056006, UM1DA051411, R33DA047032, R61DA047032, R01DA051889 and U01DA0502. K.M.F. was supported by 2UL1TR001442-08 (CTSA).

Data availability

All data that support the findings of the present study are available from the corresponding authors upon request. RNA-seq, ChIP–seq, ATAC-seq, scRNA-seq and Hi-C datasets generated in the current study were deposited in the Gene Expression Omnibus (GEO) with accession codes GSE211817, GSE211818, GSE211819, GSE211820, GSE232064 and GSE235645. The published datasets used were GSE93127, GSM5029339 and GSE109467. Source data are provided with this paper.

References

1. Friedl P & Weigelin B Interstitial leukocyte migration and immune function. Nat. Immunol. 9, 960–969 (2008). [PubMed: 18711433]
2. Rowat AC et al. Nuclear envelope composition determines the ability of neutrophil-type cells to passage through micron-scale constrictions. J. Biol. Chem. 288, 8610–8618 (2013). [PubMed: 23355469]
3. Kalukula Y, Stephens AD, Lammerding J & Gabriele S Mechanics and functional consequences of nuclear deformations. Nat. Rev. Mol. Cell Biol. 23, 583–602 (2022). [PubMed: 35513718]
4. Georgopoulos K In search of the mechanism that shapes the neutrophil's nucleus. Genes Dev. 31, 85–87 (2017). [PubMed: 28202537]
5. Nasmyth K & Haering CH Cohesin: its roles and mechanisms. Annu. Rev. Genet. 43, 525–558 (2009). [PubMed: 19886810]
6. Cavaillon J The historical milestones in the understanding of leucocyte biology initiated by Elie Metchnikoff. J. Leuc. Biol. 90, 413–424 (2011).
7. Metchnikoff E Über eine Sprosspilzkrankheit der Daphnien. Beitrag zur Lehre über den Kampf der Phagozyten gegen Krankheitserreger. Arch. Pathol. Anat. Physiol. Klin. Med. 96, 177–195 (1884).
8. Schultze M Ein heizbarer Objecttisch und seine Verwendung bei Untersuchungen des Blutes. Arch. Mikrosc. Anat. 1, 1–42 (1865).
9. Hoffmann K et al. Mutations in the gene encoding the lamin B receptor produce an altered nuclear morphology in granulocytes (Pelger–Huët anomaly). Nat. Genet. 31, 410–414 (2002). [PubMed: 12118250]

10. Shultz LD et al. Mutations at the mouse ichthyosis locus are within the lamin B receptor gene: a single gene model for human Pelger–Huët anomaly. Hum. Mol. Gen. 12, 61–69 (2003). [PubMed: 12490533]
11. Bolzer A et al. Three-dimensional maps of all chromosomes in human male fibroblast nuclei and prometaphase rosettes. PLoS Biol. 3, e157 (2005). [PubMed: 15839726]
12. Hoencamp C et al. 3D genomics across the tree of life reveals condensing II as a determinant of architecture type. Science 372, 984–989 (2021). [PubMed: 34045355]
13. Keenan CR et al. Chromosomes distribute randomly to, but not within, human nuclear lobes. iScience 24, 102161 (2021). [PubMed: 33665577]
14. Waugh B et al. Three-dimensional deconvolution processing for STEM cryotomography. Proc. Natl Acad. Sci. USA 117, 27374–27380 (2020). [PubMed: 33077585]
15. Sedat JW et al. A proposed unified interphase nucleus chromosome structure: preliminary preponderance of evidence. Proc. Natl Acad. Sci. USA 119, e2119107119 (2022). [PubMed: 35544689]
16. Lieberman-Aiden E et al. Comprehensive mapping of long-range interactions reveals folding principles of the human genome. Science 326, 289–293 (2009). [PubMed: 19815776]
17. Dixon, et al. Topological domains in mammalian genomes identified by analysis of chromatin interactions. Nature 485, 376–380 (2012). [PubMed: 22495300]
18. Hafner A et al. Loop stacking organizes genome folding from TADs to chromosomes. Mol. Cell 83, 1377–1392 (2021).
19. Yatskevich S, Rhodes J & Nasmyth K Organization of chromosomal DNA by SMC complexes. Annu. Rev. Genet. 53, 445–482 (2019). [PubMed: 31577909]
20. Schwartzer W et al. Two independent modes of chromatin organization revealed by cohesin removal. Nature 551, 51–56 (2017). [PubMed: 29094699]
21. Rao SS et al. A 3D map of the human genome at kilobase resolution reveals principles of chromatin looping. Cell 159, 1665–1680 (2014). [PubMed: 25497547]
22. Haarhuis JH et al. The cohesin release factor WAPL restricts chromatin loop extension. Cell 169, 693–707 (2017). [PubMed: 28475897]
23. Sykes DB & Kamps MP Estrogen-dependent E2A/Pbx1 myeloid cell lines exhibit conditional differentiation that can be arrested by other leukemic oncoproteins. Blood 98, 2308–2318 (2001). [PubMed: 11588024]
24. Zhu Y et al. Comprehensive characterization of neutrophil genome topology. Genes Dev. 31, 141–153 (2017). [PubMed: 28167501]
25. Grieshaber-Bouyer R et al. The neutrotime transcriptional signature defines a single continuum of neutrophils across biological compartments. Nat. Commun. 12, 2856 (2021). [PubMed: 34001893]
26. Zhu Y, Denholtz M, Lu H & Murre C Calcium signaling instructs NIPBL recruitment at active enhancers and promoters via distinct mechanisms to reconstruct genome compartmentalization. Genes Dev. 35, 65–81 (2021). [PubMed: 33334824]
27. Nabet B et al. The dTAG system for immediate and target-specific protein degradation. Nat. Chem. Biol. 14, 431–441 (2018). [PubMed: 29581585]
28. Khoyratty TE et al. Distinct transcription factor networks control neutrophil-driven inflammation. Nat. Immunol. 22, 1093–1106 (2021). [PubMed: 34282331]
29. Hu Y et al. Super-enhancer reprogramming drives a B cell-epithelial transition and high-risk leukemia. Genes Dev. 30, 1971–1990 (2016). [PubMed: 27664237]
30. Heinz S et al. Simple combinations of lineage-determining transcription factors prime cis-regulatory elements required for macrophages and B cell identities. Mol. Cell 38, 576–589 (2010). [PubMed: 20513432]
31. Martinon F, Burns K & Tschopp J The inflammasome: a molecular platform triggering activation of inflammatory caspases and processing of proIL-β. Mol. Cell 10, 417–426 (2002). [PubMed: 12191486]
32. Thomas PG et al. The intracellular sensor NLRP3 mediates key innate and healing responses to influenza A virus via the regulation of caspase-1. Immunity 30, 566–575 (2009). [PubMed: 19362023]

33. Li MT et al. Negative regulation of RIG-I mediated innate antiviral signaling by SEC14L1. J. Virol. 87, 10037–46 (2013). [PubMed: 23843640]
34. Braunholz D et al. Isolated NIPBL-missense mutations that cause Cornelia de Lange syndrome alter MAU2 interaction. Eur. J. Hum. Genet. 20, 271–276 (2012). [PubMed: 21934712]
35. Chao WCH et al. Structural studies reveal the functional modularity of the Scc2-Scc4 cohesin loader. Cell Rep. 12, 719–725 (2015). [PubMed: 26212329]
36. Seki A & Rutz S Optimized RNP transfection for highly efficient CRISPR/Cas9-mediated gene knockout in primary T cells. J. Exp. Med. 215, 985–997 (2018). [PubMed: 29436394]
37. Hendel A et al. Chemically modified guide RNAs enhance CRISPR–Cas genome editing in human primary cells. Nat. Biotechnol. 33, 985–989 (2015). [PubMed: 26121415]
38. Xie X et al. Single-cell transcriptome profiling reveals neutrophil heterogeneity in homeostasis and infection. Nat. Immunol. 21, 1119–1133 (2020). [PubMed: 32719519]
39. Rao SS et al. Cohesin loss eliminates all loop domains. Cell 171, 305–320 (2017). [PubMed: 28985562]
40. Calderon L et al. Cohesin-dependence of neuronal gene expression relates to chromatin loop length. eLife 11, e76539 (2022). [PubMed: 35471149]
41. Cuartero S et al. Control of inducible gene expression links cohesin to hematopoietic progenitor self-renewal and differentiation. Nat. Immunol. 9, 932–941 (2018).
42. Kalukula Y, Stephens AD, Lammerding J & Gabriele S Mechanisms and functional consequences of nuclear deformations. Nat. Rev. Mol. Cell Biol. 23, 583–602 (2022). [PubMed: 35513718]
43. Mohana G et al. Chromosome-level organization of the regulatory genome in the *Drosophila* nervous system. Cell 186, 3826–3844 (2023). [PubMed: 37536338]
44. Bashkirova E & Lomvardas S Olfactory receptor genes make the case for interchromosomal interactions. Curr. Opin. Genet. Dev. 55, 106–113 (2019). [PubMed: 31491591]
45. Hu Y et al. Lineage specific 3D genome organization is assembled at multiple scales by Ikaros. Cell 186, 5260–5289 (2023).

References

46. Andrews S FastQC: a quality control tool for high throughput sequence data. Babraham Bioinformatics http://www.bioinformatics.babraham.ac.uk/projects/fastqc (2010).
47. Dobin A et al. STAR: ultrafast universal RNA-seq aligner. Bioinformatics 29, 15–21 (2013). [PubMed: 23104886]
48. Robinson MD et al. edgeR: a Bioconductor package for differential expression analysis of digital gene expression data. Bioinformatics. 26, 139–40 (2010). [PubMed: 19910308]
49. Raudvere U et al. gProfiler: a web server for functional enrichment analysis and conversion of gene lists. Nucleic Acids Res. 47, W191–W198 (2019). [PubMed: 31066453]
50. Yu G, Wang L & He Q ChIPseeker: an R/Bioconductor package for ChIP peak annotation, comparison and visualization. Bioinformatics 31, 2382–2383 (2015). [PubMed: 25765347]
51. Robinson JT et al. Integrative genomics viewer. Nat. Biotechnol. 29, 24–26 (2011). [PubMed: 21221095]
52. Zhang, et al. Fast alignment and preprocessing of chromatin profiles with Chromap. Nat. Commun. 12, 6566 (2021). [PubMed: 34772935]
53. Yang, et al. .HiCRep: assessing the reproducibility of HiC data using a stratum-adjusted correlation coefficient. Genome Res. 11, 1939–1949 (2017).
54. Kuleshov MV et al. Enrichr: a comprehensive gene set enrichment analysis web served 2016 update. Nucleic Acids Res. 44, W90–W97 (2016). [PubMed: 27141961]
55. Hao Y et al. Integrated analysis of multimodal single-cell data. Cell 184, 3573–3587 (2021). [PubMed: 34062119]
56. Blondel VD, Guillaume J-L, Lambiotte R & Lefebvre E Fast unfolding of communities in large networks. J. Stat. Mech. Theory Exp. 2008, P10008 (2008).
57. Lange M et al. CellRank for directed single-cell fate mapping. Nat. Methods 19, 159–170 (2022). [PubMed: 35027767]

58. Gulati GS et al. Single-cell transcriptional diversity is a hallmark of developmental potential. Science 367, 405–411 (2020). [PubMed: 31974247]

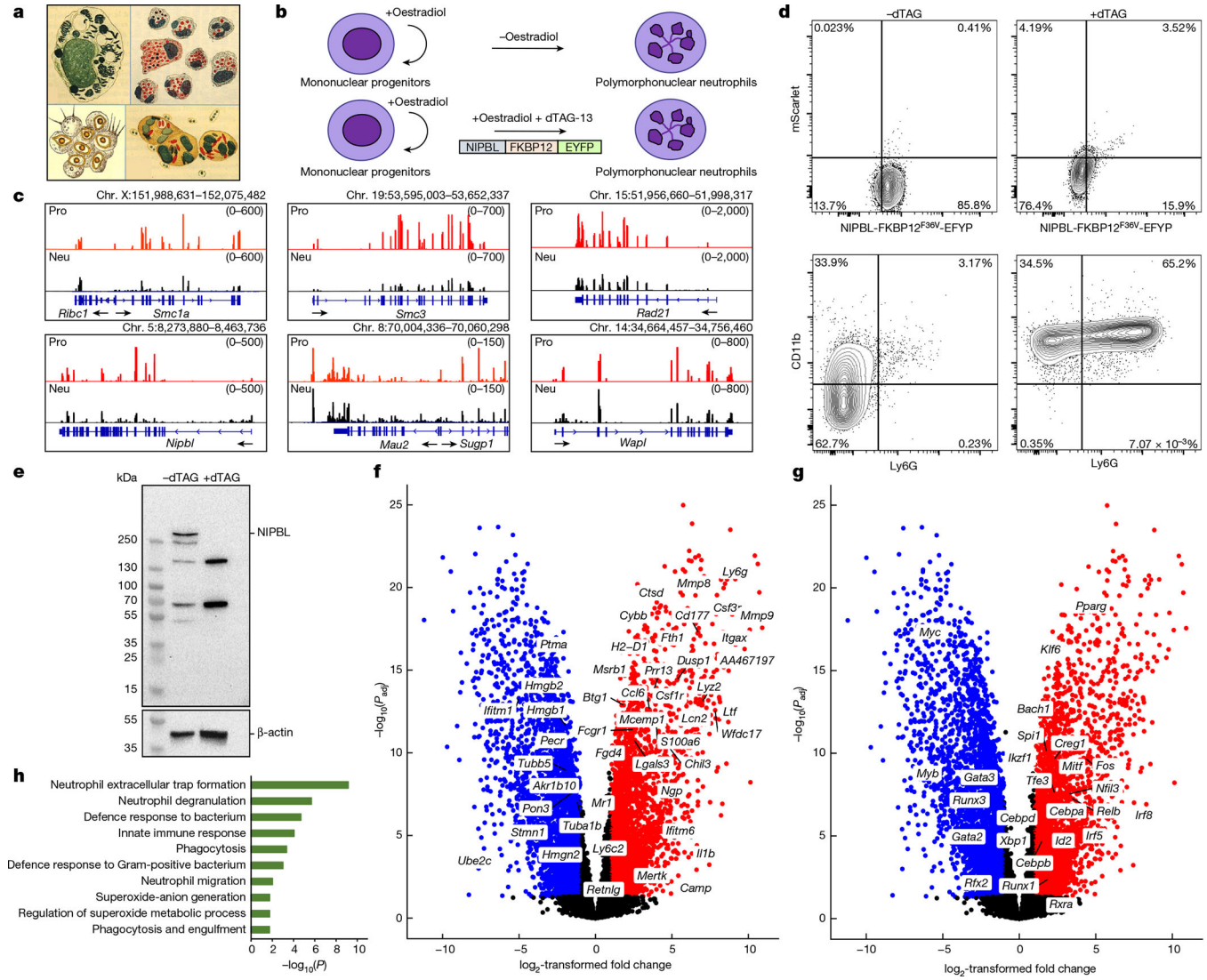

Fig. 1 |. Halting loop extrusion activates a neutrophil-specific gene program.

a, Drawings of polymorphonuclear leukocytes by E. Metchnikoff, reproduced with permission from ref. 6, Oxford Univ. Press. **b**, Model system to identify mechanisms that underpin the assembly of polymorphonuclear structures. NIPBL-FKBP12^{F36V}-EYFP cells cultured with β-oestradiol remained mononuclear and undifferentiated, whereas withdrawing β-oestradiol induced neutrophil differentiation. When NIPBL-FKBP12^{F36V}-EYFP cells were cultured in the presence of β-oestradiol and dTAG-13, the abundance of NIPBL acutely declined to orchestrate the differentiation of polymorphonuclear cells. **c**, RNA sequencing (RNA-seq) tracks indicate the abundance of mRNAs encoding loop-extrusion factors in ECOMG progenitors (Pro; red) and in ECOMG-derived differentiated neutrophils (Neu; black). **d**, NIPBL-FKBP12^{F36V}-EYFP ECOMG progenitors were cultured for 72 h with β-oestradiol and in the absence or presence of dTAG-13, and examined for the expression of NIPBL–EYFP, CD11b and Ly6G. **e**, Western blot analysis of the expression of NIPBL in NIPBL-FKBP12^{F36V}-EYFP ECOMG progenitors cultured for 72 h with β-oestradiol and in the absence or presence of dTAG-13. **f**,**g**, Depletion of NIPBL

activates a neutrophil-specific transcription signature. Volcano plots highlight neutrophil-signature genes (**f**) and genes encoding transcription factors (**g**) associated with neutrophil differentiation in NIPBL-depleted cells. Upregulated genes are indicated in red (adjusted *P* value (P_{adj}) < 0.05 and $\log_2$-transformed fold change > 1); downregulated genes are shown in blue (P_{adj} < 0.05 and $\log_2$-transformed fold change < −1). **h**, Gene ontology (GO)-based functional classification of differentially expressed genes that were upregulated in cells depleted for NIPBL. The data were obtained from three independent biological replicates.

a

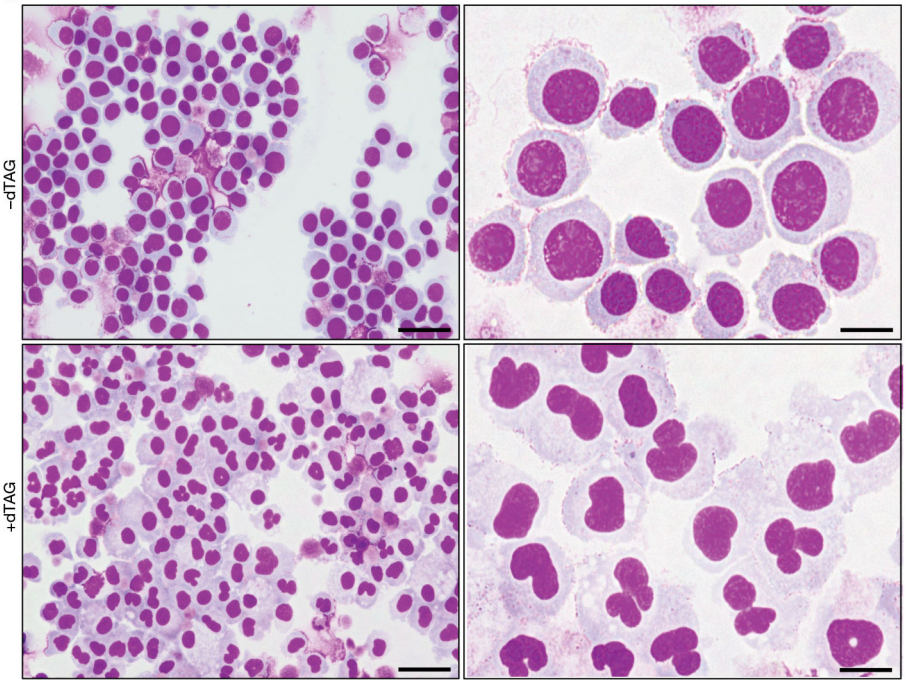

b

–dTAG (NIPBL-FKBP12^{F36V}-EFYP)

	DC1	DC2	DC3	DC4	DC5	Average
Precursors	98	99	99	98	99	98.6%
Myelocytes	2	1	1	2	1	1.4%
Metamyelocytes	0	0	0	0	0	0%
Band neutrophils	0	0	0	0	0	0%
Mature neutrophils	0	0	0	0	0	0%
Hypersegmented neutrophils	0	0	0	0	0	0%
Total cells	100	100	100	100	100	100%

+dTAG (NIPBL-FKBP12^{F36V}-EFYP)

	DC1	DC2	DC3	DC4	DC5	Average
Precursors	30	37	39	35	27	33.6%
Myelocytes	43	48	45	48	52	47.2%
Metamyelocytes	11	4	5	4	9	6.6%
Band neutrophils	1	0	1	1	0	0.6%
Mature neutrophils	4	5	4	2	7	4.4%
Hypersegmented neutrophils	11	6	6	10	5	7.6%
Total cells	100	100	100	100	100	100%

Fig. 2 |. Depletion of NIPBL leads to the assembly of polymorphonuclear structures.

a, Wright–Giemsa staining of NIPBL-FKBP12^{F36V}-EYFP ECOMG cells cultured with β-oestradiol alone (top) or with both β-oestradiol and dTAG-13 (bottom). Objectives used were 40× (left) and 100× (right). Scale bars, 20 μm (left) and 10 μm (right). **b**, Tables listing the percentages of mononuclear precursor cells, myelocytes, metamyelocytes, band neutrophils, mature neutrophils and hypersegmented neutrophils. DC, differential counts.

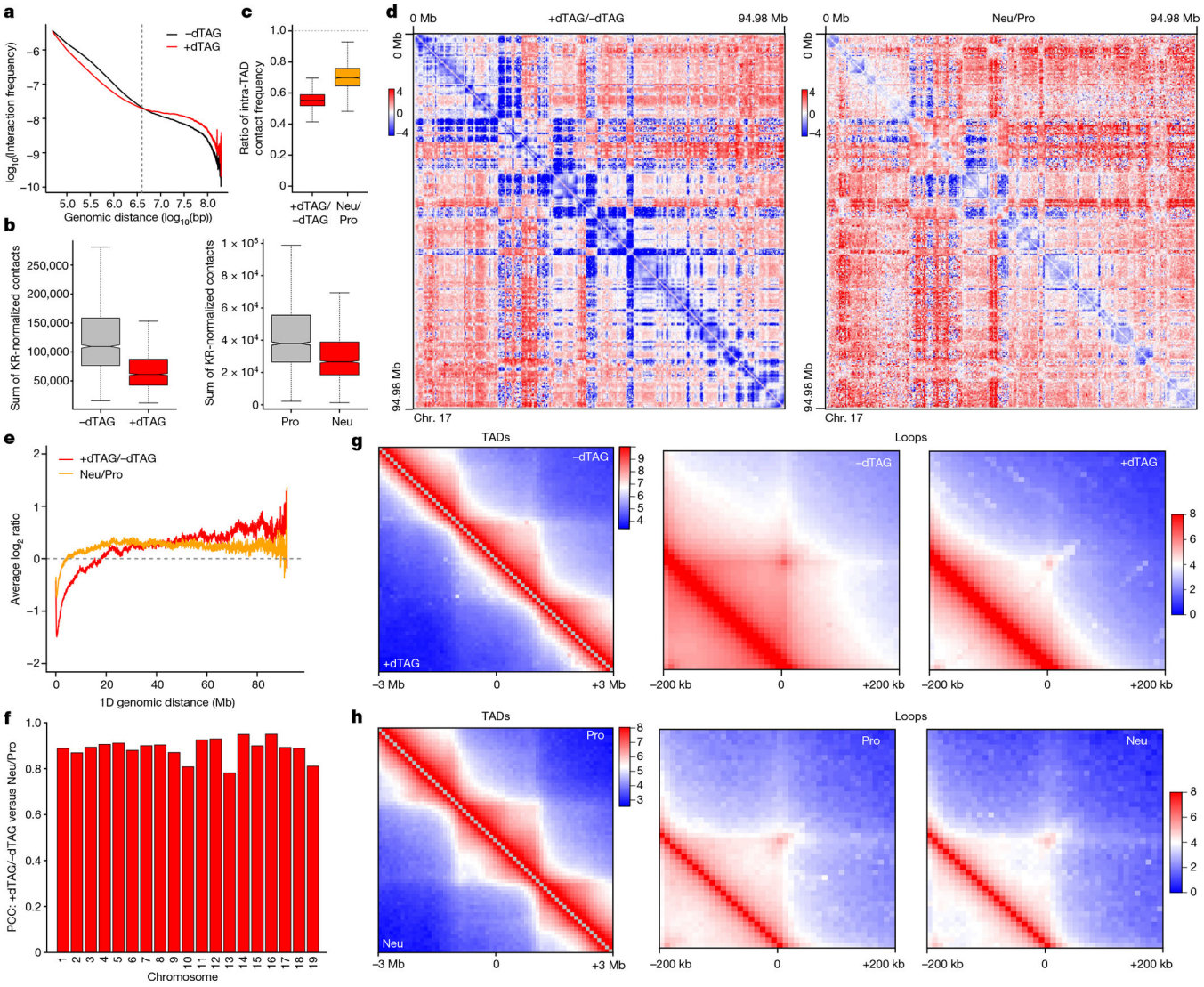

Fig. 3 |. Halting loop extrusion produces a chromatin architecture that mirrors that of differentiated neutrophils.

a, Hi-C contact probability plot showing the average intrachromosomal contact frequency as a function of genomic distance for ECOMG progenitors (−dTAG-13) and NIPBL-depleted ECOMG progenitors (+dTAG-13). **b**, Box plots showing the sum of KR-normalized intra-TAD Hi-C contact frequencies (50 kbp resolution) for NIPBL-FKBP12^{F36V}-EYFP ECOMG cells grown in the absence or in the presence of dTAG-13. $P < 2.2 \times 10^{-16}$ (two-sided paired *t*-test comparing cells cultured in the presence of dTAG-13 versus those cultured in its absence). In each box, the top edge, horizontal centre line and bottom edge represent the 75th percentile, median and 25th percentile, respectively. The top whiskers represent the 75th percentile + 1.5× the interquartile range (IQR). The bottom whiskers represent the 25th percentile − 1.5× the IQR. **c**, Box plots showing the ratio of intra-TAD interaction frequencies for the indicated cell types and culture conditions. $P < 2.2 \times 10^{-16}$ (two-sided two-sample *t*-test). Statistics as described above. **d**, Heat maps showing differential intrachromosomal contact frequencies across chromosome 17

(250 kbp resolution) for the indicated cell types and culture conditions. **e**, Average $\log_2$ ratios of KR-normalized Hi-C intrachromosomal contact frequencies of chromosome 17 (50-kbp resolution) calculated for ECOMG progenitors (−dTAG-13) versus NIPBL-depleted ECOMG progenitors (+dTAG-13), as well as for ECOMG progenitors (+oestradiol; Pro) versus ECOMG-derived differentiated neutrophils (−oestradiol; Neu) (Pearson correlation coefficient (PCC) value = 0.6582). **f**, PCC values for individual chromosomes in indicated cell types and conditions, computed for average $\log_2$ ratios of KR-normalized Hi-C intrachromosomal contact frequencies that were stratified for genomic distance. NIPBL-FKBP12^{F36V}-EYFP cells cultured in the absence versus the presence of dTAG-13 were compared with NIPBL-FKBP12^{F36V}-EYFP progenitors cultured in the presence (Pro) versus the absence (Neu) of oestradiol. **g**, Left, meta-TAD plot for NIPBL-FKBP12^{F36V}-EYFP cells cultured in the absence versus the presence of dTAG-13, showing average KR-normalized contact frequencies for TADs (1 Mb) across 3-Mb windows (n = 99). Right, meta-loop plots showing average KR-normalized contact frequencies for loops that span 200 kbp (n = 313). Meta-loop plots are shown for NIPBL-FKBP12^{F36V}-EYFP cells cultured in the absence or presence of dTAG-13. **h**, Left, meta-TAD plot for NIPBL-FKBP12^{F36V}-EYFP cells cultured in the presence (Pro) versus the absence (Neu) of oestradiol, showing average KR-normalized contact frequencies for TADs (1 Mb) across 3-Mb windows (n = 84). Right, meta-loop plots showing average KR-normalized Hi-C contact frequencies calculated for loops that span 200 kbp (n = 57). Meta-loop plots are shown for NIPBL-FKBP12^{F36V}-EYFP progenitors and NIPBL-FKBP12^{F36V}-EYFP-derived neutrophils.

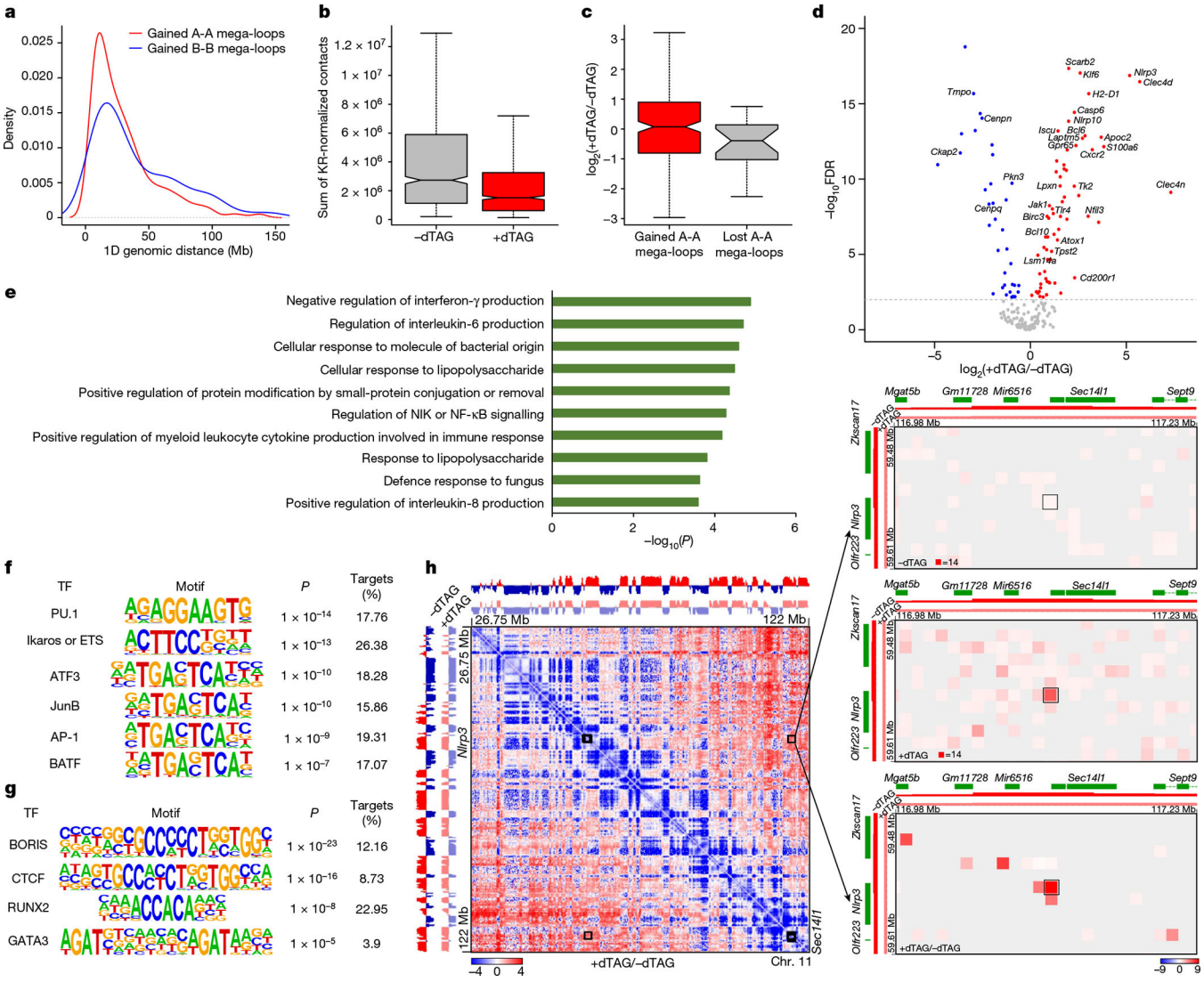

Fig. 4 |. Halting loop extrusion induces the assembly of mega-loops.

a, Density plots showing the distribution of genomic distances for gained A-A (red) and gained B-B (blue) mega-loops. **b**, Mega-loop bodies are depleted of intra-TAD genomic interactions in NIPBL-depleted cells. $P < 2.2 \times 10^{-16}$ (two-sided paired *t*-test comparing NIPBL-FKBP12^{F36V}-EYFP cells cultured in the absence of dTAG-13 versus those cultured in its presence). **c**, Box plots showing transcript abundance (measured as $\log_2$(FPKM + 1) at anchors of gained (217 genes) and lost (21 genes) mega-loops. **d**, Volcano plot showing the change in transcript abundance, measured in $\log_2$(FPKM + 1) (*x* axis) versus $-\log_{10}$ false discovery rate (FDR) (*y* axis), for 217 genes located at genomic regions that span anchors (10-kbp resolution) of gained mega-loops in NIPBL-depleted cells. **e**, GO enrichment analysis for genomic regions that span tethers of gained mega-loops in NIPBL-depleted cells. NIK, NF-κB-inducing kinase. **f**,**g**, Transcription factor (TF) motif enrichment analysis of gained (**f**) and lost (**g**) ATAC-seq sites at anchors of de novo mega-loops in NIPBL-FKBP12^{F36V}-EYFP cells cultured in the absence versus the presence of dTAG-13. **h**, Heat map indicating differential intrachromosomal contact frequencies across chromosome 11

(250-kbp resolution) in NIPBL-FKBP12^{F36V}-EYFP cells cultured in the presence versus the absence of dTAG-13. Gain and loss of contact frequencies are shown as red pixels and blue pixels, respectively. Heat maps indicate an intrachromosomal interaction hub involving the *Nlrp3* and *Sec14l1* loci (10-kbp resolution).